Constraints on the Feasibility of Ferrovolcanism on Asteroid 16 Psyche

Jorritsma, J. J.; van Westrenen, W.

DOI
10.1029/2024JE008811

Publication date
2025

Document Version
Final published version

Published in
Journal of Geophysical Research: Planets

JGR Planets

RESEARCH ARTICLE

10.1029/2024JE008811

Constraints on the Feasibility of Ferrovolcanism on Asteroid 16 Psyche

J. J. Jorritsma[1,2] and **W. van Westrenen**[1]

[1]Department of Earth Sciences, Faculty of Science, Vrije Universiteit Amsterdam, Amsterdam, The Netherlands, [2]Now at Faculty of Aerospace Engineering, TU Delft, Delft, The Netherlands

Key Points:

- Boundary conditions to achieve ferrovolcanism on Psyche are quantified
- The entire formation history of Psyche must be taken into account to assess the probability of these conditions being met

Correspondence to:

J. J. Jorritsma,
j.jorritsma@tudelft.nl

Citation:

Jorritsma, J. J., & van Westrenen, W. (2025). Constraints on the feasibility of ferrovolcanism on asteroid 16 Psyche. *Journal of Geophysical Research: Planets*, *130*, e2024JE008811. https://doi.org/10.1029/2024JE008811

Received 7 NOV 2024
Accepted 16 JUL 2025

Author Contributions:

Conceptualization: J. J. Jorritsma, W. van Westrenen
Investigation: J. J. Jorritsma
Methodology: J. J. Jorritsma
Project administration: W. van Westrenen
Software: J. J. Jorritsma
Supervision: W. van Westrenen
Validation: J. J. Jorritsma
Visualization: J. J. Jorritsma
Writing – original draft: J. J. Jorritsma
Writing – review & editing: J. J. Jorritsma, W. van Westrenen

Abstract Asteroid 16 Psyche's surface appears to be highly metallic, but its bulk density suggests a silicate-rich interior. Ferrovolcanism has been suggested to explain how a silicate-rich body could develop a metallic surface. This requires trapping of light elements bearing iron-rich metallic melt in a core solidifying from the outside inwards. The buoyancy of the lighter melt must then generate sufficient pressure to carry metal melt through the mantle and cover the surface. Here, we test whether sufficient pressure could have been generated on 16 Psyche in different scenarios. Core size, light element partitioning between mantle and core, and silicate mass loss are calculated for three meteoritic bulk compositional models (H-chondrite, EH-chondrite and mesosiderite) based on mantle density and mantle porosity combinations. The resulting core compositions are used to calculate excess pressure. Mantle density and porosity combinations leading to ferrovolcanism are constrained for each bulk composition. Iron-rich bulk compositions with low light element abundances are favored. Mesosiderite bulk composition is most conducive to producing ferrovolcanism but does not naturally fit the ferrovolcanism framework. Primitive compositions are favored as the timing of ferrovolcanism is tied to the earlier stages of solar system formation. H-chondrite model scenarios may produce ferrovolcanism but require high amounts of mass loss to be considered as a building block for Psyche. EH-chondrite model scenarios are chemically not conducive to producing ferrovolcanism. Both confirmation and rejection of the ferrovolcanism hypothesis by upcoming observations from NASA's Psyche mission can therefore provide key new constraints on 16 Psyche origin and evolution scenarios.

Plain Language Summary Asteroid 16-Psyche, the largest M-type asteroid, appears to have a significant amount of metal on its surface. Its density is not high enough to be fully metallic which leads to questions on the origin of the metal-rich surface. A recent hypothesis invokes ferrovolcanism as the responsible process. This mechanism starts with a metallic core and silicate mantle. If the core solidifies from the outside in, a solid outer core shell can encapsulate lighter metallic magma in the center. The density difference between the molten inner core and solid outer core generates a buoyant pressure that can break apart the outer core and the mantle, carrying molten metal to the surface. This work tests whether sufficient buoyant pressure can be generated for a variety of bulk compositions and mantle properties of Psyche. Core size, composition and density are calculated for each model to assess buoyant pressure generation. Bulk compositions with lower density struggle to produce sufficient excess pressure as the cores that can be produced are small, as a consequence of their low iron content. Higher density building blocks with high iron contents are more conducive to generating sufficient pressures to carry metallic melt from 16-Psyche's inner core to the surface.

1. Introduction

Asteroid 16 Psyche (hereafter simply referred to as "Psyche") is the largest M-type asteroid and the 10th most massive asteroid in our solar system, accounting for ~1% of the mass of the main asteroid belt (Polanskey et al., 2018). To estimate Psyche's shape and size, Shepard et al. (2021) combined a large data set of radar observations, advanced optics images and stellar occultations. This yielded a shape model approximating a tri-axial ellipsoid with major axis lengths of 278 (−4/+8) km, 238 (−4/+6) km and 171 (−1/+5) km for the *a*-, *b*- and *c*-axis respectively. The axis of rotation corresponds to the *c*-axis. The shape model has a volume of 5.73 (−0.08/+0.31) × 10^6 km^3. The most recent mass estimate is based on the mutual deflection after close encounters with other bodies, yielding a mass of 2.399 ± 0.025 × 10^{19} kg (Farnocchia et al., 2024). These combine to give Psyche a bulk density estimate of 4,187 (−240/+86) kg/m^3.

Psyche is classified as an M-type asteroid in Tholen's taxonomy (Tholen, 1984) based on its relatively featureless red-sloped surface reflectance spectra with moderate optical albedo in the visible wavelength region. Due to similarities with enstatite chondrites and iron meteorites, these reflectance features are thought to be indicative of a surface with a high metallic fraction. This originated the hypothesis that Psyche and other M-type asteroids are the exposed or disrupted cores of differentiated planetesimals (Binzel et al., 1995).

Analysis of a broader wavelength range revealed a weak absorption feature at ∼0.9 μm, commonly linked to a low-Fe, low-Ca orthopyroxene component. The surface abundance estimates of this component range from 0% to 20%, with the rest of the surface consisting of metal (Becker et al., 2020; Cantillo et al., 2021; Cloutis et al., 2009; Fornasier et al., 2010; Hardersen et al., 2011; Landsman et al., 2018). Mercury and asteroid 21 Lutetia produce similar optical reflectance spectra but have entirely silicate surfaces based on MESSENGER and Rosetta mission data, respectively (Coradini et al., 2011; Domingue et al., 2010; McClintock et al., 2008).

The radar albedo of Psyche's surface is high, with an average value of 0.34 ± 0.08 (Shepard et al., 2021), consistent with a high surface metal fraction (Elkins-Tanton et al., 2020). There is significant variation in the radar albedo of Psyche's rotation, with individual measurements ranging from 0.22 to 0.52. The lower boundary registers at the high end of C- and S-class asteroids' radar albedos (Magri et al., 2007). The upper end of this range is only rivaled by M-type asteroid 758 Mancunia with a radar albedo of 0.55 ± 0.14 (Shepard et al., 2015) and possibly 216 Kleopatra with a radar albedo of 0.43 ± 0.10 over its southern hemisphere (Shepard et al., 2018). These high radar reflectivity values are found on the southern hemisphere of Psyche and appear to be correlated to areas of optical albedo reflectivity (Shepard et al., 2021). The large range of radar albedo measurements suggests significant variation in the surface metal abundance or surface density over Psyche's rotation (Elkins-Tanton et al., 2020).

A possible anti-correlation is observed between the absorption band depth and radar albedo during a full rotation of Psyche (Sanchez et al., 2016); a higher band depth, likely caused by an increased abundance of the ortho-pyroxene component, corresponds to a lower radar albedo, likely caused by a decreased metallic abundance. Similarly, a positive correlation between the spectral slope and radar albedo was observed. Higher values for both are interpreted to be caused by an increased surface metallic abundance (Sanchez et al., 2016).

Cambioni et al. (2022) fit thermal emission data from ALMA to a model with variable thermal inertia and dielectric constants. They found that most of Psyche's surface has both a thermal inertia and dielectric constant that are indicative of a metal-rich material in the uppermost few millimeters. The bulk density of Psyche is too low for it to be a predominantly metallic body. With the meteoric Fe-Ni mineral kamacite having a 1 atm density of 7,870 kg/m^3, a bulk porosity of ∼50% would be required if Psyche consists mostly of this metal (Elkins-Tanton et al., 2020). Nichols-Fleming et al. (2022) modeled the viscous pore space closure of a pure iron body through time at different starting porosities and temperatures and concluded that a Psyche-sized metallic core must have cooled to and remained below an upper limit of 800 K to retain a bulk porosity of >50%. At any temperature above this limit, iron bodies rapidly lose most of their bulk porosity on a Myr timescale, with an iron body of >850 K retaining <10% of its porosity. If Psyche is a cooled rubble pile, models indicate that the required ∼50% porosity can be supported by cold-welding ∼1 m size metallic boulders (Zhang et al., 2022).

An intact differentiated planetesimal with a core of the mass of Psyche would require a minimum cooling time of more than 100 Myr (Bryson et al., 2015; Nichols-Fleming et al., 2022; Tarduno et al., 2012). A stripped core with the mass of Psyche would require a minimum of 10 Myr to cool to 800 K (Scheinberg et al., 2016). Any porosity-adding impact must therefore have occurred at least 10 Myr after a mantle stripping event for the metallic core to retain a significant amount of porosity. Potential porosity adding collisions, such as hit-and-run collisions or the subsequent catastrophic impact phase, are tied to the early phases of solar system accretion, before planetesimals become massive enough for most impacts to result in perfect mergers (Bonsor et al., 2015; Cambioni et al., 2021; Chambers, 2013). Catastrophic impacts are supposedly the cause of the disruption of ordinary chondrites' parent bodies which took place at or near those parent bodies' peak temperatures (Lucas et al., 2020). These temperatures are expected to be reached prior to the 10 Myr mark post CAI-formation (Bouvier et al., 2007). As Psyche's 10 Myr minimum required cooling period likely exceeds the hit-and-run collision and catastrophic impact phases of the solar system formation, Nichols-Fleming et al. (2022) deem it unlikely that such collisions could be the cause of Psyche's inferred ∼50% porosity, should it indeed be predominantly metallic.

In the absence of a younger porosity-adding event, the core is assumed to have little to no porosity. This implies the presence of a significant non-metal component in Psyche, as including a non-metal component of lower density is required to achieve Psyche's present-day bulk density. If the core has little to no porosity, the bulk porosity is limited as the non-metal component is the only contributor to Psyche's bulk porosity. This limit on bulk porosity further increases the required volume fraction of the non-metal component (Elkins-Tanton et al., 2020).

In summary, Psyche's main characteristics are enigmatic; the bulk density requires a significant non-metal mantle, but the surface appears to be highly metallic. This led to the inception of the ferrovolcanism model, first by Abrahams and Nimmo (2019) for a fully metallic body and later adapted by Johnson et al. (2020) to include a mantle.

The model by Johnson et al. (2020) relies on having an initially fully molten metallic core solidified from the outside in. The solidifying outer core is assumed to comprise of FeNi dendrites, trapping interconnected regions of progressively light-element enriched melt, with sulfur considered the only light element by Johnson et al. (2020). The density difference between the FeNi dendrites and the trapped melt increases as the outer core continues to solidify and the melt enriches in S. This density difference generates sufficient excess pressure to overcome the yield strength of the mantle, creating ferromagmatic dykes. If sufficient excess pressure is generated to overcome the negative buoyancy of the S-rich metallic melt in the mantle as well, the dykes can reach the surface, resulting in the ferrovolcanism that covers parts of the surface in molten metal.

The viability of the ferrovolcanism mechanism is necessarily limited to the early stages of Psyche's history, when the core was solidifying. Ferrovolcanic units are therefore likely mixed with silicates in regolith produced by impacts over billions of years (Johnson et al., 2020). This could provide the origin of the lowest radar albedo measurements on Psyche's surface, equivalent to the highest silicate asteroids' radar albedo measurements. If ferrovolcanism occurred preferentially in the southern hemisphere, a remnant of high-volume ferrovolcanic units could be the cause for the high radar albedo in this hemisphere.

The effect of light elements other than S, the available amount of melt that can be trapped in the dendritic outer core growth, as well as the portion of this melt that could be expelled on the surface, were not explored in the Johnson et al. (2020) study. Alternatively, as the outer core solidifies, the molten inner core also gets progressively enriched in light elements. The buoyant pressure generated here may also be sufficient to overcome the yield strength of the outer core, thereby creating a pathway to the core-mantle boundary (CMB) where it can continue to intrude into the mantle (Johnson et al., 2020). The goal of this study is to quantify conditions under which sufficient pressure can be generated in the molten inner core to overcome the yield strength of the outer core and the mantle, as well as the negative buoyancy of metallic melt in the silicate mantle, in order to produce ferrovolcanism on Psyche. Additional light element partitioning and chemical constraints are also considered.

Three meteorite compositions were used as end member models for Psyche's bulk chemical composition. The widest possible range of input parameters is tested for each composition, in an attempt to evaluate the likelihood that ferrovolcanism is indeed the cause for Psyche's enigmatic characteristics.

2. Methods

To quantify whether sufficient excess pressure is generated, Psyche's core size, mantle thickness and core composition need to be calculated for each model scenario. This study's model simplifies Psyche's shape to a perfect ellipsoid with the primary axis lengths of 278, 238, and 171 km and corresponding volume of 5.924×10^6 km^3. The core is assumed to be perfectly centered and is given the same axial ratios as the total body to retain an equal mass distribution (Figure 1).

The considered endmember meteorite building blocks of Psyche are an ordinary chondrite, an enstatite chondrite and a mesosiderite, with the used bulk compositions presented in Jorritsma and van Westrenen (2025).

Ordinary chondrites are the most common meteorites. Of the ordinary chondrites, the H-chondrite has the highest Fe content, making this the ordinary chondrite composition that is most conducive to producing ferrovolcanism. It has a grain density (i.e., bulk density in the absence of porosity) of 3,640 kg/m^3 (Britt & Consolmagno, 2003).

The enstatite meteorite composition is chosen as this is interpreted to be the source for asteroid 21 Lutetia (Drummond et al., 2018), the only M-type asteroid to be visited by a spacecraft so far. This work considers an EH-group enstatite. It has a grain density of 3,670 kg/m^3 (Britt & Consolmagno, 2003). Enstatite chondrite

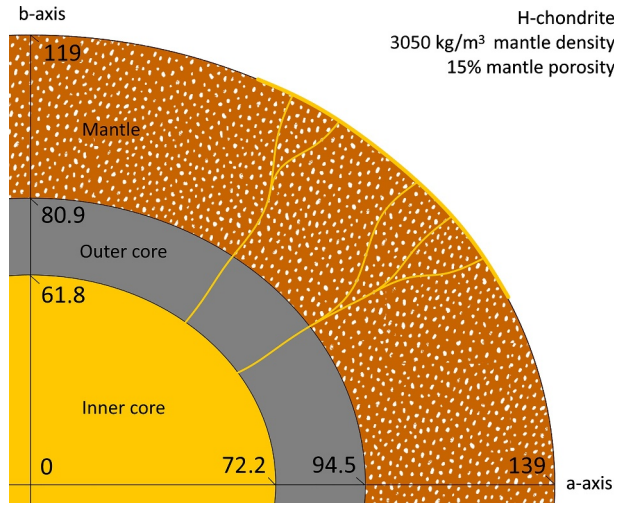

Figure 1. Schematic representation of the ferrovolcanism mechanism for one of the model scenarios. Numbers on the axes indicate the radii of the molten inner core, solid outer core and mantle in km from the center of the core on the *a*- and *b*-axes. White texture indicates mantle porosity.

compositions crystallize low-FeO pyroxenes first when solidified (McCoy et al., 1999), placing them in the lower regions of the mantle. This matches Psyche's spectral properties if later formed mantle minerals are preferentially stripped in mass loss (Section 1).

Ferrais et al. (2020) theorize that Psyche's current shape is the remnant of a Jacobi ellipsoid, the result of solidification from a fully molten state caused by a later giant impact. This allows non-primitive meteorite compositions to be considered in the ferrovolcanism framework. Here, mesosiderites are considered a possibility based on the match with Psyche's density and supposed pyroxene composition, although Libourel et al. (2023) concluded that Psyche's low fraction of surface pyroxene was not compatible with a mesosiderite-like surface. A grain density of 4,400 kg/m^3 is used (Britt & Consolmagno, 2003).

The core composition is based on the calculated metal-silicate partitioning of C, O, S, Ni, P and Si. It is assumed that this partitioning equilibrated under mantle liquidus conditions, simulating core differentiation and light element partitioning from a fully molten state in the early stages of solar system solidification.

The metal-silicate partitioning equation from Steenstra et al. (2017) is used for P, partitioning equations from Steenstra & van Westrenen (2018) are used for C, O, S and Ni;

$$\log D_P^{\text{met-sil}} = 1.75(\pm0.72) - 1.25\left(2\log\left(\frac{\chi_{\text{FeO}}^{\text{sil}}}{\chi_{\text{Fe}}^{\text{met}}}\right) + 2\log\left(\frac{\gamma_{\text{FeO}}^{\text{sil}}}{\gamma_{\text{Fe}}^{\text{met}}}\right)\right) - 2.81(\pm0.76)\chi_{\text{MgO}}^{\text{sil}} + 22.54(\pm4.42)\chi_{\text{Al}_2\text{O}_3}^{\text{sil}} - 10.22(\pm0.95)\chi_{\text{CaO}}^{\text{sil}} + 2.71(\pm1.01)\chi_{\text{FeO}}^{\text{sil}} - \frac{6068(\pm1011)}{T} + 469(\pm118)\left(\frac{P}{T}\right) + 4.18(\pm0.52)\ln\left(1-\chi_S^{\text{met}}\right) \quad (1)$$

$$\log D_C^{\text{met-sil}} = 2.26 + \frac{2920}{T} + 115\left(\frac{P}{T}\right) - 0.66\left(\frac{\text{nbo}}{t}\right) - 0.15\left(2\log\left(\frac{\chi_{\text{FeO}}^{\text{sil}}}{\chi_{\text{Fe}}^{\text{met}}}\right) + 2\,log\left(\frac{\gamma_{\text{FeO}}^{\text{sil}}}{\gamma_{\text{Fe}}^{\text{met}}}\right)\right) - 2.9\chi_{Ni}^{\text{met}} - 0.17\chi_{\text{H}_2\text{O}}^{\text{sil}} \quad (2)$$

$$\log D_O^{\text{met-sil}} = 2.19(\pm0.53) - \frac{10731(\pm1329)}{T} + 33(\pm18)\left(\frac{P}{T}\right) + \log\left(\frac{\chi_{\text{FeO}}^{\text{sil}}}{\chi_{\text{Fe}}^{\text{met}}}\right) - \log\left(\frac{\gamma_{\text{O}}^{\text{met}}}{\gamma_{\text{Fe}}^{\text{met-1}}}\right) \quad (3)$$

$$\log D_S^{\text{met-sil}} = -3.30(\pm0.47) + \frac{3000(\pm1023)}{T} + 33(\pm11)\left(\frac{P}{T}\right) + \log\left(\chi_{\text{FeO}}^{\text{sil}}\right) - \log\left(C_S\right) + 14(\pm2)\,ln\left(1-\chi_O^{\text{met}}\right) \quad (4)$$

$$\log D_{\mathrm{Ni}}^{\mathrm{met-sil}} = 0.46(\pm 0.16) + \frac{2700(\pm 300)}{T} - 61(\pm 6)\left(\frac{P}{T}\right) + \log\left(\frac{\chi_{\mathrm{FeO}}^{\mathrm{sil}}}{\chi_{\mathrm{Fe}}^{\mathrm{met}}}\right) - \log\left(\frac{\gamma_{\mathrm{Ni}}^{\mathrm{met}}}{\gamma_{\mathrm{Fe}}^{\mathrm{met}}}\right) \quad (5)$$

$D_i^{\mathrm{met-sil}}$ is the partition coefficient between the metallic core and silicate mantle of element i. χ_{ox}^{sil} represents the molar fraction of oxide ox in the silicate mantle. χ_i^{met} represents the molar fraction of element i in the metallic core. P (in GPa) and T (in K) are the pressure and temperature at which partitioning occurred. $\left(\frac{\mathrm{nbo}}{t}\right)$ is the number of non-bridging oxygen anions per tetrahedrally coordinated cation, a parameter calculated from the mantle composition (Mysen et al., 1982). Equation 4 depends on the C_S term, representing the sulfide capacity which incorporates the effect of oxygen fugacity on S partitioning (Steenstra & van Westrenen, 2018). This parameter is calculated from the silicate melt composition and regression parameters reported by Haughton et al. (1974);

$$\log(C_S) = -5.704 + 3.15(\pm 0.64)\,\chi_{\mathrm{FeO}}^{\mathrm{sil}} + 2.65\,(\pm 0.56)\,\chi_{\mathrm{CaO}}^{\mathrm{sil}} + 0.12(\pm 0.38)\,\chi_{\mathrm{MgO}}^{\mathrm{sil}} + 0.77(\pm 0.91)\,\chi_{\mathrm{TiO_2}}^{\mathrm{sil}} + 0.75(\pm 0.58)\,\chi_{\mathrm{Na_2O+K_2O}}^{\mathrm{sil}} \quad (6)$$

$\gamma_{ox}^{\mathrm{sil}}$ and γ_i^{met} are activity coefficients which are assumed to be unity (Doyle et al. (2019). This eliminates the activity terms from all equations.

Partitioning for Si is calculated using the partitioning equation from Steenstra & van Westrenen (2020);

$$\log K_{\mathrm{app}}^{\mathrm{met-sil}}\mathrm{Si}^{4+} = \log\frac{\left(\chi_{\mathrm{FeO}}^{\mathrm{sil}}{}^{2} * \chi_{\mathrm{Si}}^{\mathrm{met}}\right)}{\left(\chi_{\mathrm{SiO_2}}^{\mathrm{sil}} * \chi_{\mathrm{Fe}}^{\mathrm{met}}\right)} + \log\frac{\left(\gamma_{\mathrm{Si}}^{\mathrm{met}}\right)}{\left(\gamma_{\mathrm{Fe}}^{\mathrm{met}}\right)^2} + \log\frac{\left(\gamma_{\mathrm{FeO}}^{\mathrm{sil}}\right)^2}{\left(\gamma_{\mathrm{SiO_2}}^{\mathrm{sil}}\right)}, \quad (7)$$

with $K_{\mathrm{app}}^{\mathrm{met-sil}}Si^{4+}$ representing the apparent exchange coefficient of Si^{4+} between the metallic core and silicate mantle. Again, the activity coefficients are set to unity. This equation was parameterized by Steenstra & van Westrenen (2020) for the 0–5 GPa range as;

$$\log K_{\mathrm{app}}^{\mathrm{met-sil}}\mathrm{Si}^{4+} = 2.23(\pm 0.82) - \left(\frac{17409(\pm 1420)}{\mathrm{T}}\right) + 509(\pm 108)\left(\frac{P}{T}\right) - 0.7(\pm 0.07)\left(\frac{\mathrm{nbo}}{t}\right) \quad (8)$$

Equation 8 is used to calculate the value for $\log K_{\mathrm{app}}^{\mathrm{met-sil}}Si^{4+}$ which can then be used to calculate $\chi_{\mathrm{Si}}^{\mathrm{met}}$ by rewriting Equation 7;

$$\chi_{\mathrm{Si}}^{\mathrm{met}} = \frac{K_{\mathrm{app}}^{\mathrm{met-sil}}\mathrm{Si}^{4+} * \chi_{\mathrm{SiO_2}}^{\mathrm{sil}} * \chi_{\mathrm{Fe}}^{\mathrm{met}}}{\chi_{\mathrm{FeO}}^{\mathrm{sil}}{}^{2}} \quad (9)$$

For simplicity, the error margins in each of the partitioning equations and the calculation of the C_S parameter are ignored. Only the reported center values are used.

There are multiple feedback mechanisms within this set of equations (Equations 1–9). The $\left(\frac{\mathrm{nbo}}{t}\right)$ and C_S parameters are calculated from the abundances of mantle oxides that depend on the total partitioning, as some of the considered mantle constituents partition between the mantle and the core. $\chi_{\mathrm{Fe}}^{\mathrm{met}}$ depends on the partitioned amounts of all light constituents, on the mass of the core and on how much Fe is required to fill out this mass. $\chi_{\mathrm{FeO}}^{\mathrm{sil}}$ depends on the distribution of Fe between the mantle and the core. The partitioning of S depends on the partitioning of O as it includes the $ln\left(1 - \chi_O^{\mathrm{met}}\right)$ term. Similarly, the partitioning of P depends on $ln\left(1 - \chi_S^{\mathrm{met}}\right)$ and the partitioning of C on $\chi_{\mathrm{Ni}}^{\mathrm{met}}$. To resolve these feedback loops, all parameter calculations are performed iteratively until convergence to a balanced state. A constant metal-silicate equilibration temperature of 2050 K was used throughout the partitioning calculations. This value approximates the peridotite liquidus temperature at the low pressures expected for a body of Psyche's size and mass (Jennings & Holland, 2015). With this temperature and a calculated pressure, core composition and mantle composition, all partition coefficients can be calculated for use in the core composition calculations of the next iteration. When the iterative process has converged (typically within 10

iterations), the resulting core composition is used to calculate the attainable excess pressure from trapping metallic melt in the inner core. All steps in the model calculations are further outlined below.

2.1. Core Size and Mantle Thickness

The first step in the iterative process is to calculate the core and mantle volume fractions using a mass balance equation;

$$\rho_b = f_c * \rho_c * (1 - \varphi_c) + f_m * \rho_m * (1 - \varphi_m) \tag{10}$$

With ρ_b, ρ_c, and ρ_m denoting the bulk, core grain and mantle grain densities respectively. f_c and f_m represent the core and mantle volume fractions and φ_c and φ_m represent the core and mantle porosities. The core porosity is assumed 0 because of viscous pore space closure (Nichols-Fleming et al., 2022).

The difference in volume between Psyche's most recent shape model and the model's perfect ellipsoid representation of present-day Psyche is accredited to mass deficit regions in the shape model, assumed to be mass loss regions where lighter mantle material was stripped. To account for the additional light material in the model, the bulk density ρ_b is set to 4,150 kg/m^3, slightly lower than the measured present-day value of 4,187 kg/m^3.

The core density was calculated from the core composition of the previous iteration. With the bulk density known and the core porosity disregarded, the mantle grain density and mantle porosity are the only remaining variables. When these are chosen, the core and mantle volume fractions can be calculated by rewriting Equation 10, given that f_m is equal to $1 - f_c$;

$$f_c = \frac{\rho_b - \rho_m * (1 - \varphi_m)}{\rho_c - \rho_m * (1 - \varphi_m)} \tag{11}$$

The a-axis radius of the core can be calculated using a rewritten version of the volume of an ellipsoid;

$$a = \sqrt[3]{\frac{3}{4} V_P * f_c / \left(\frac{b}{a} * \frac{c}{a} * \pi\right)} \tag{12}$$

where a is the a-axis core radius, V_P is Psyche's ellipsoidal volume of 5.924×10^6 km^3, f_c is the calculated core volume fraction and $\frac{b}{a}$ and $\frac{c}{a}$ are the b- and c-axis length ratios with the a-axis length, respectively. The b- and c-axis radii can be calculated by multiplying the calculated a-axis radius by these ratios. The mantle thickness on each axis is calculated by subtracting the core radius from the total radius.

2.2. Mass Loss and Pressure

The core and mantle volume fractions and chosen mantle porosity can be used to calculate Psyche's grain density ρ_g as;

$$\rho_g = \frac{\rho_b}{(1 - \varphi_b)} = \frac{\rho_b}{f_c + f_m * (1 - \varphi_m)} \tag{13}$$

Each considered meteoritic bulk composition has a given grain density. The difference in grain density between Psyche and the meteorite used is used to calculate a hypothetical mass loss (illustrated in Figure 2). The assumption is made that a volume of meteoritic material produces a differentiated body with the same grain density as the meteorite building block. The mantle has a grain density below the meteorite's grain density. Stripping away mantle material therefore increases the grain density of the remainder (Figure 2). The volume of mantle material that needs to be stripped to increase the meteorite's grain density to Psyche's current grain density can be calculated as;

$$V_L = \frac{V_g * (\rho_g - \rho_{\text{met}})}{\rho_{\text{met}} - \rho_m} \tag{14}$$

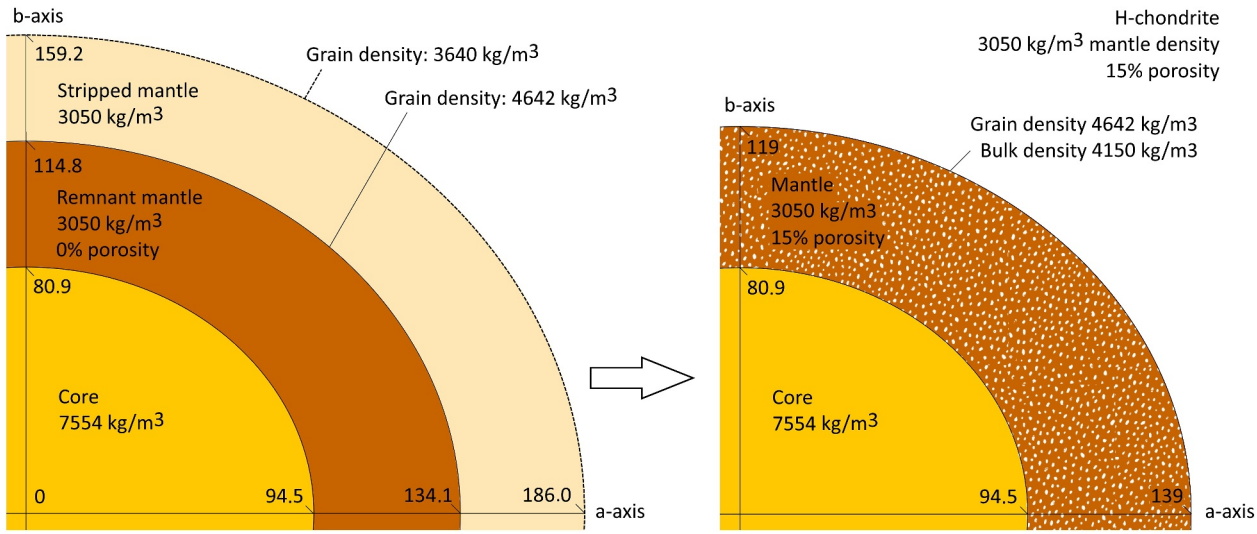

Figure 2. Mass loss schematic of an H-chondrite model scenario with a mantle density of 3,050 kg/m^3 and a mantle porosity of 15%. The core density was calculated in the iterative process. Numbers on the axes indicate the radii in km from the center of the core on the *a*- and *b*-axes. Left: Pre-mass loss model without mantle porosity. The grain density of the original body (dashed line) is equal to the meteorite grain density: 3,640 kg/m^3. The mantle is stripped until the remnant has a grain density of 4,642 kg/m^3. Right: adding 15% mantle porosity to the remnant mantle reduces the grain density of 4,642 kg/m^3 to Psyche's current bulk density of 4,150 kg/m^3 and increases the remnant body to Psyche's current size. White texture indicates mantle porosity. 52.7% of the original mass is lost in this model scenario.

where V_L is the volume of mantle material lost, V_g is Psyche's grain volume (equal to $V_P * (1 - \varphi_b)$), ρ_g is Psyche's grain density, ρ_{met} is the meteorite grain density and ρ_m is the mantle grain density.

With a mantle grain density closer to the grain density of the meteorite, more mantle stripping has to be reversed to close the gap between the asteroid and meteorite grain densities. Higher porosities produce higher grain densities for Psyche (Equation 13), increasing the density gap with the meteorite and the required mass loss.

The volume of mantle material lost is used to calculate the original size and mass of Psyche, before any mantle material was stripped as well as the original core mass and volume fractions. These are used to calculate the CMB pressure. The metal-silicate equilibration pressure was set to the pressure at the CMB. This pressure is calculated from the body's gravitational acceleration;

$$g = G * \frac{m}{r^2} \tag{15}$$

where g is the gravitational acceleration, G is the universal gravitational constant and m is the mass contained within distance r from the center of the body. At the CMB, m is the mass of the core and r is the radius of the core. At the surface, m is the original mass and r is the radius corresponding to the original grain volume (Figure 2). The mantle porosity is set to zero for this step, as it represents a fully molten state in which porosity cannot persist.

Since the ellipsoid model has variable radii for the core and for Psyche as a whole, the core and mantle are simplified to a volume equivalent perfect sphere in which pressure is even over the CMB. Using the original grain volume and core volume fraction, along with their respective volume equivalent spherical radii, the gravitational acceleration is calculated at the CMB and Psyche's surface with Equation 15. The difference between the gravitational acceleration at the surface and CMB is converted to a pressure gradient over the thickness of the mantle, which is used to calculate the pressure at the CMB.

2.3. Core Composition and Core Density

For the first iteration, the core is assumed to consist solely of Fe with a density of 7,900 kg/m^3. This iteration yields the first partition coefficients for the core's lighter constituents P, Ni, S, O, C and Si that are used to calculate the core composition for the next iteration.

P, Ni, S, O and C partitioning behavior is quantified by calculating metal-silicate partition coefficients $D_i^{\text{met-sil}}$ (Equations 1–5). These are used to calculate the core mass fraction of each element with a simple mass balance approach (Rai & van Westrenen, 2014), where, in the case of siderophile elements, for every $\left(D_i^{\text{met-sil}} + 1\right)$ atoms of element i in the bulk composition, $D_i^{\text{met-sil}}$ atoms partition to the core and 1 remains in the mantle. The partitioning fraction is used to calculate the mass fraction of the total body that is situated in the core. Dividing by the core mass fraction gives the mass fraction of the element in the core;

$$i_C = \left(\frac{D_i^{\text{met-sil}}}{D_i^{\text{met-sil}} + 1} * i_b\right) / m_C \tag{16}$$

where i_C is the mass fraction of element i in the core, i_b is the mass fraction of element i in the bulk composition and m_C is Psyche's original core mass fraction. The core mass fractions of P, Ni, S, O, and C were calculated in this way. The remainder of the core mass is filled with Fe. These core mass fractions are converted to molar fractions.

The molar fraction of Si in the core is calculated using Equations 8 and 9. The mass fractions of P, Ni, S, O and C in the core should be unaffected, so the calculated molar fraction of Si takes the place of Fe. Therefore, the molar fraction of Fe is lowered by a mass equivalent amount of the molar fraction of Si. More moles of Si are added than moles of Fe taken out because Fe is heavier than Si, so the previously calculated molar fractions of P, Ni, S, O and C along with the lowered molar fraction of Fe and the added molar fraction of Si are renormalized to 100%. The calculated core molar fractions are used in various partitioning equations. The partitioning equations of P, C, O, Ni and Si depend on $\chi_{\text{Fe}}^{\text{met}}$. The partitioning of C further depends on $\chi_{\text{Ni}}^{\text{met}}$, the partitioning of S depends on $\chi_{\text{O}}^{\text{met}}$ and the partitioning of P depends on $\chi_{\text{S}}^{\text{met}}$.

To calculate the density of the core composition, the molar fractions of each light element alloyed with Fe were calculated. The considered endmembers are Fe, FeO, Fe_3C, Fe_3P, FeS, FeNi and FeSi. The core density ρ_C is calculated using ideal mixing equations of these alloys;

$$\rho_C = \frac{\mu_{\text{mix}}}{V_{\text{mix}}} = \frac{\Sigma \chi_i * \mu_i}{\Sigma \chi_i * V_i} \tag{17}$$

where μ_{mix} is the molar mass of the mix, V_{mix} is the unit-cell volume of the mix and χ_i, μ_i and V_i are the core molar fractions, molar masses and unit-cell volumes of each of the light elements' Fe alloys. Room-temperature and room-pressure unit-cell volumes are used as these are readily available (Li et al., 2002; Montes-Arango et al., 2016; Pachmayr et al., 2016; Scott et al., 2007; Vočadlo et al., 2002; Yu & Ji, 2017). This represents the present-day cooled core density. This density is used in the following iteration for the core size (Section 2.1) and subsequent mass loss and pressure calculations (Section 2.2).

2.4. Mantle Composition

The mantle composition is mainly used in the calculation of the $\left(\frac{\text{nbo}}{t}\right)$ and C_S parameters as well as compositional parameters for the partitioning of P (Equation 1). The $\left(\frac{\text{nbo}}{t}\right)$ parameter is calculated from the mass fractions of the main mantle forming oxide components, normalized to 100%, in accordance with Mysen et al. (1982). The considered oxide components are FeO, Na_2O, MgO, Al_2O_3, SiO_2, P_3O_5, K_2O, CaO, TiO_2, MnO, Cr_2O_3, and NiO. The C_S parameter is calculated from molar fractions of a selection of these oxides (Equation 6).

The total mass fractions of the lithophile elements Na, Mg, Al, Ca, Ti, Mn, and Cr in the model bulk compositions are divided by Psyche's mantle mass fraction to calculate each element's mass fraction in the mantle. Fe, P, Si, and Ni partly partition to the core. For these elements, the mass fraction of the total that partitions to the core is subtracted from the bulk composition before calculating the mantle remnant. Elemental mass fractions are converted to moles/100 g of mantle material. These values are converted to moles/100 g of each element's respective oxides with the assumption that sufficient oxygen is available for each. These are normalized to 100%, representing molar fractions in the mantle. Molar fractions are converted to mass fractions.

With the mantle composition calculated in both molar and mass fractions, a chosen temperature of 2,050 K, the CMB pressure calculated in Section 2.2 and the core composition calculated in Section 2.3, all parameters in each

partition coefficient equation are now available. The resulting partition coefficients are used in the core and mantle composition calculations of the next iteration.

The calculations outlined in Sections 2.1-2.4 are repeated for each iteration, until the process produces an iteration that does not differ significantly from the previous. The process is deemed complete when each calculated data field in an iteration is equal to the previous iteration within 0.1‰. This is usually attained by the 10th iteration. The results of the 100th iteration are reported. By this iteration, all model scenarios are within the 0.1‰ boundary from the previous iteration. The core size, mantle thickness and core composition of this iteration are then used to calculate the excess pressure as detailed below. An open-source Excel spreadsheet that can be used for all calculations are provided in Jorritsma and van Westrenen (2025).

2.5. Excess Pressure Calculations

The excess pressure generated by trapping melt in the inner core is calculated as follows;

$$P_e = \Delta\rho_{(\text{solid}-\text{melt})} h g \tag{18}$$

where P_e is the excess pressure, $\Delta\rho_{(\text{solid}-\text{melt})}$ is the density contrast between the solid outer core and molten inner core, h is the column height of interconnected melt in the outer core and g is the gravitational acceleration at the CMB (as calculated following Section 2.2).

In this study's framework, wherein the buoyant pressure of trapped melt in the inner core first has to overcome the yield strength of the outer core, the column height spans the entire radius of the outer core. The outer core is assumed to grow concentrically inward without incorporating any other constituents besides Fe and Ni. The volume of the outer core dictates the column height in the excess pressure calculations. Excess pressure is therefore largest when all of the available Fe is solidified.

Fe in the core is firstly used in alloys with the light elements. These alloys have binary eutectic compositions taken from the literature (Fe-S: Breuer et al. (2015); Fe-O: Steinberg et al. (1998); Fe-C: Pollack (1998); Fe-Si: Meco and Napolitano (2005); Fe-P: Zaitsev et al. (1995)). All alloys are treated separately, each requiring a different amount of additional Fe for a eutectic composition. The Fe required for light element alloys and their eutectic compositions is, in our model, the minimum required amount of Fe in the inner core melt. The Fe that is not used in either the light element alloys or their eutectic compositions is considered as available for outer core solidification ("free Fe"). This allows for a Fe–Ni outer core to grow. A supereutectic core composition is possible above the eutectic temperature but would not be conducive to producing ferrovolcanism, because in this case the resulting outer core would consist of light element Fe alloys with a much lower density than an Fe-Ni outer core.

Ni is the only minor constituent that this work considers to partition between the solid outer and molten inner cores. Ni has a solid metal-molten metal partition coefficient $D_{\text{Ni}}^{\text{solid}-\text{melt}} \cong 1$ regardless of pressure or molten metal sulfur content (Stewart et al., 2009). Therefore, the distribution of Ni is calculated to have an equal molar fraction in the solid outer core and molten inner core. The molar abundances of the light elements, their eutectic Fe and alloy Fe are calculated, as well as the molar abundance of free Fe. Ni is then distributed by the ratio of the free Fe compared to the total reservoir of the other light elements, their eutectic Fe and alloyed Fe. The outer core consists of this Ni alloyed with Fe and all free Fe that is not used in the alloys or eutectic compositions of the other light constituents.

The molten inner core consists of all the P, S, C, O and Si and the remaining Ni in the core composition, with enough Fe for each light element's respective alloy and eutectic composition. In the presence of sufficient other light elements (>1 wt%), two immiscible liquids are formed when the S concentration reaches ~5 wt% (Bercovici et al., 2022 and references therein, Bromiley et al., 2024). Since all light elements are enriched to their eutectic compositions by outer core solidification, these mass fractions are easily attained in the molten inner core. It is therefore assumed that an immiscible low-density sulfide liquid forms in every model scenario, separated from the rest of the inner core due to its buoyancy (Bercovici et al., 2022). This liquid is used as the melt source for ferrovolcanism (Figure 3).

With decreasing pressure, the immiscible sulfide liquid contains less additional light elements, which are largely concentrated in the sulfur-poor liquid. Dasgupta et al. (2009) show this immiscible liquid relation in a Fe–C–S

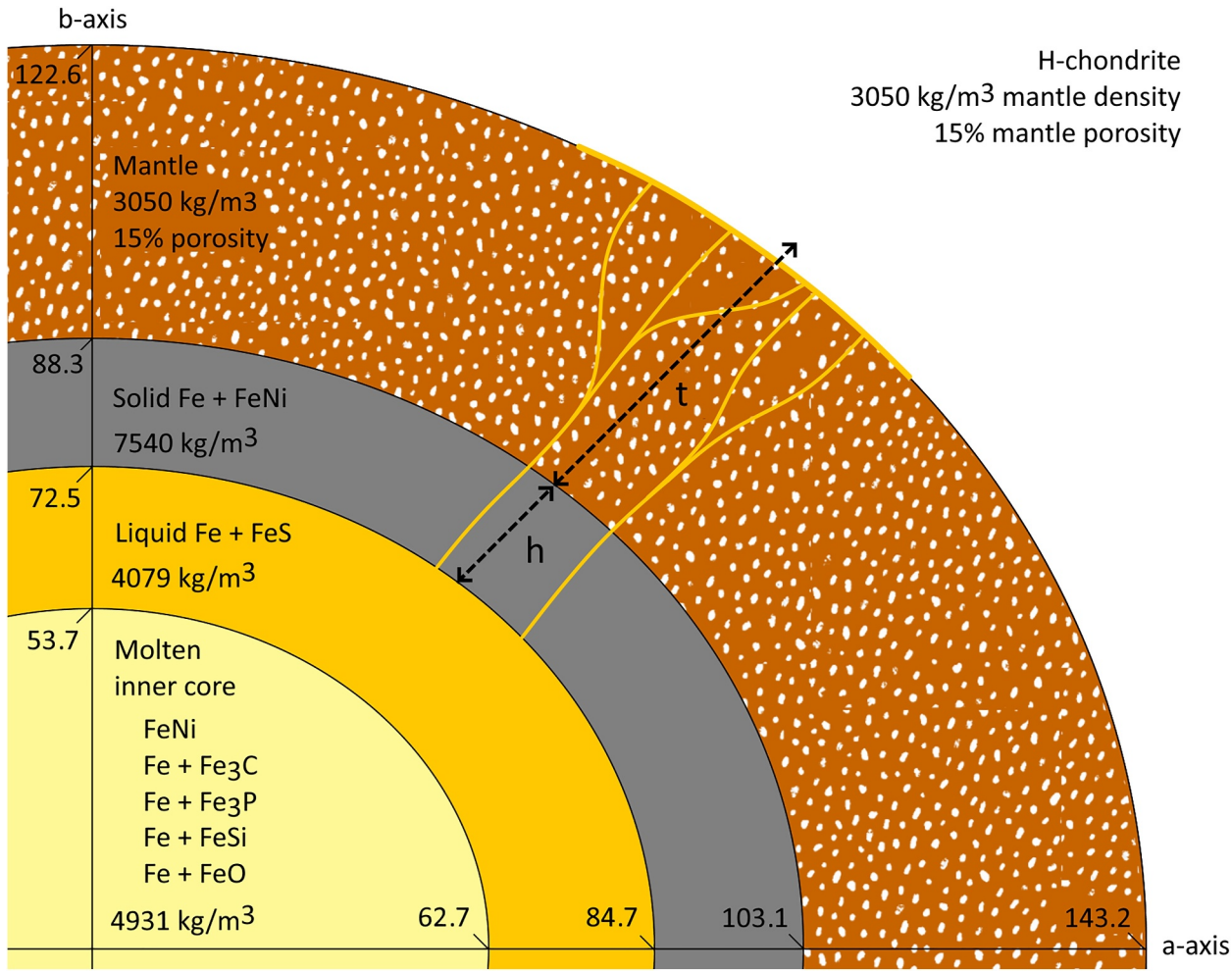

Figure 3. Schematic representation of inner core separation and excess pressure generation for the H-chondrite model with a mantle density of 3,050 kg/m^3 and a mantle porosity of 15%. The solid outer core and molten inner core density were calculated from their respective compositions and adjusted for thermal expansion. Column height h spans the thickness of the outer core. This model scenario results in a penetration ratio of 1.07; penetration height t is higher than the mantle thickness, so ferrovolcanism can be achieved. Numbers on the axes indicate the radii of the thermal expansion corrected volumes of each layer on the a- and b-axis in km from the center of the core.

system. The sulfide-rich immiscible liquid contains molar fractions of ~16%, 7%, and 3% C at 5 GPa, 4 and 2 GPa, respectively. The calculated CMB pressure in Psyche for the bulk compositions rarely considered exceeds 0.05 GPa. Bromiley et al. (2024) experimentally determined the immiscibility in the $Fe_{0.9}Ni_{0.1}$-S-P-O-C system, resulting in a separate FeS-rich melt and an Fe-rich melt with P and C. O is potentially distributed between the two liquids in 0.5 and 1 GPa experiments. We assume for our low-pressure model scenarios that the sulfide immiscible liquid contains all of the sulfur in the core in an eutectic composition with no additional light elements. This leaves the sulfur-poor immiscible liquid with all other light elements and no sulfur.

The molar fractions of Fe, FeS, Fe_3C, Fe_3P, FeNi, FeSi, and FeO for the entire core are known (Section 2.3). These are separated into Fe + FeNi for the outer core, a eutectic Fe + FeS for the sulfide layer and Fe + Fe_3C + Fe_3P + FeNi + FeSi + FeO for the inner core, accounting for Fe that is used in each alloy's eutectic composition. The room-temperature density of each layer is calculated using the ideal mixing relation that was used to calculate the core density (Section 2.3). The molar fractions of the total core are converted to mass fractions of the total core for each layer. The total core mass is known, so the mass of each layer can be calculated. Each layer's volume can be calculated from their respective mass and density.

These densities and volumes are representative of the current core in its fully cooled state. The outer core volume is assigned a thermal expansion factor of 1.045, based on a temperature increase of 900 K and a thermal

expansivity of 0.00005 per K (Chopelas & Boehler, 1992). This gives the outer core a total temperature near the eutectic temperature of Fe + FeS (1261 K at low pressure, Breuer et al., 2015). The calculated outer core density is decreased by the same thermal expansion factor.

Johnson et al. (2020) used a parameterized equation to calculate the density of Fe-S melts at 1900 K;

$$\rho_{\mathrm{Fe-S}} = 6950 - 5176\chi - 3108\chi^2 \tag{19}$$

where χ is the molar fraction of S in the FeS melt. The eutectic composition of Fe + FeS at low pressure is 31 wt% S (Breuer et al., 2015), equivalent to a molar fraction of 0.439 S. $\rho_{\mathrm{Fe-S}}$ is therefore equal to 4,079 kg/m^3.

Using the ideal mixing relation (Equation 17), a eutectic Fe + FeS layer is calculated to have a room-temperature density of 6,593 kg/m^3. This gives the eutectic Fe + FeS layer a thermal expansion factor of 1.616 between its current cooled state and molten state at 1261 K. This expansion factor is applied to the immiscible sulfide layer as well as the rest of the inner core, in order to more accurately calculate the solid outer core thickness (Figure 3). This thickness is calculated similar to the mantle thickness calculations (Section 2.1).

The density contrast between the eutectic Fe + FeS melt density of 4,079 kg/m^3 and the outer core density corrected for thermal expansion is used in the excess pressure calculation (Equation 18). This excess pressure should overcome the yield strength of warm Fe as well as the tensile strength of the mantle (<10 MPa and ~0.5–6 MPa, respectively. Johnson et al., 2020).

If both of these are overcome, ferromagmatic dikes of eutectic sulfide composition can propagate through the mantle. The melt is denser than the mantle, so the excess pressure has to be sufficient to overcome the negative buoyancy of the melt in the mantle. The penetration height can be calculated by equating the excess pressure to the negative buoyancy of the melt in the mantle;

$$P_e = \Delta\rho_{(\mathrm{melt-mantle})} t g \tag{20}$$

where $\Delta\rho_{(\mathrm{melt-mantle})}$ is the density contrast between the eutectic Fe + FeS melt and the mantle, including the mantle porosity, and t is the penetration height (Figure 3). The gravitational acceleration g at the CMB is used again (Section 2.2). The effect of increasing gravitational acceleration with distance from the core center is ignored as the difference is small, in accordance with Johnson et al. (2020).

The mantle is assumed to have cooled at the stage of ferrovolcanism and the mantle volume and density are therefore not corrected from the calculations in Section 2.1. The increased core volume does mean that the mantle is spread over a larger ellipsoid, so the mantle thickness on each axis is recalculated. Dividing the penetration height t by this mantle thickness gives a penetration ratio. Values of more than 1 indicate that sufficient excess pressure is generated to carry the melt through the mantle to the surface, meaning that ferrovolcanism can be achieved.

If there is no sufficient excess pressure in this scenario, more pressure can be generated by increasing the column height in the outer core. We assume progressive concentric inward core growth. No more free Fe is available, so instead this is done by solidifying parts of the immiscible sulfide liquid that resides between the outer core and the rest of the molten inner core. As detailed above, this liquid has a eutectic Fe + FeS composition. Adding solid eutectic sulfide to the outer core increases the column height but lowers the average outer core density and with it, the density contrast used in the excess pressure calculation. This partly mitigates the effect of the additional column height, so the excess pressure increase is limited. Furthermore, the available melt volume decreases as the additional outer core growth is sourced from the same layer as the ferromagmatic melt. Up to 90% of the available Fe + FeS is solidified and added to the outer core in order to assess if sufficient excess pressure can be attained in this way.

2.6. Input Parameters

In addition to the assumed bulk composition and grain density, the only input variables for our models are mantle grain density and mantle porosity. The range of plausible values for the mantle grain density and mantle porosity is; however, heavily constrained. The lower bound of the mantle grain density is governed by the core size

calculations (Section 2.1) and the methodology of the core composition calculation (Section 2.3). Lighter mantles, resulting from a low mantle grain density, require larger core mass fractions to achieve Psyche's bulk density. The mass fractions of light elements in the core are calculated from the metal-silicate partition coefficients, and the rest of the core mass is filled with Fe. However, a limited amount of Fe is available in the bulk composition. Mantles with lower densities require cores with more Fe, at some point exceeding the Fe that is available in the bulk composition.

Conversely, if the core size is too small due to high mantle grain density, it cannot contain the required amount of Fe to alloy with all the partitioned light elements and their eutectic compositions. This depends on the amounts of light elements that partition to the core as they use Fe for alloys and eutectic compositions as well as lowering the amount of Fe that fills up the rest of the core mass. Above this mantle grain density, the core is enriched beyond the eutectic composition and will not solidify an Fe-Ni outer core. Instead, light element alloys will solidify first until the remaining melt is at its eutectic composition. This results in a low-density outer core, which is not conducive to producing ferrovolcanism due to the low density contrast with eutectic Fe + FeS melt (Equation 18).

If enough Fe is present for each light element's eutectic composition, the core may still be too small. The excess pressure generated is based on the outer core thickness and should be high enough to overcome the negative buoyancy of the melt in the mantle. With smaller cores, lower outer core thicknesses are produced, resulting in lower excess pressures, while higher excess pressures are required to overcome the increased mantle thickness associated with a smaller core. Conversely, lower mantle densities are conducive to producing ferrovolcanism because the associated larger cores have more available Fe for outer core growth and less mantle to overcome.

Mass loss is used in the framework of this model in order to equate Psyche's grain density to the densities of the meteoritic building blocks. Preferential erosion of the mantle is the only form of mass loss considered in this work. This does however provide additional constraints on the mantle grain density. Psyche's grain density can only be decreased to a meteorite's grain density when reversing mass loss of lighter mantle. Psyche's current grain density therefore has to be higher than the meteorite's grain density. This means that meteoritic building blocks with a higher grain density than Psyche's bulk density (mesosiderite in this work) require a minimum mantle porosity; this increases Psyche's grain density to above the meteorite grain density. Psyche's grain density is governed by the mantle porosity, as the mantle porosity is the only contributor to Psyche's bulk porosity in this work (Equation 13). The core is assumed to have no porosity. The asteroid survey by Carry (2012) shows that asteroids with up to 10^{19} kg mass can have macroporosities ranging from 0% to 60%. A mass of 10^{20} kg is needed to compress asteroid interiors to lower porosities. Psyche approaches but does not reach this mass; therefore, this scenario cannot be ruled out on that basis (Shepard et al., 2017). Carry (2012) found that most asteroids more than 200 km in diameter have a bulk porosity of <10%. Large asteroids such as Ceres and Vesta have estimated silicate porosities similar to the upper lunar crust (<15%), implying that self-gravitation has closed the pores significantly in silicate bodies of this size (Elkins-Tanton et al., 2020). This work considers a viable mantle porosity range of 0%–25%.

The allowable range of mantle grain densities is dependent on the light element abundances and Fe abundances in the bulk composition. This range therefore differs per meteorite. The mantle porosity is tested at intervals of 2.5%.

3. Results

3.1. Partition Coefficients

The calculated CMB pressures in model runs that fall within mantle density constraints on core size (Section 2.6) range from 0.012–0.060 GPa. Most of the calculated partition coefficients are very extreme as a result, either almost all or almost none of the respective light element partitions to the core, except for P (see below). This behavior is expected at such low pressures (Bercovici et al., 2022).

Partitioning of S is high in every model scenario; the lowest calculated value for $D_S^{met-sil}$ is 35.

The partitioning of Ni incorporates the $\left(\frac{\chi_{FeO}^{sil}}{\chi_{Fe}^{met}}\right)$ parameter. Larger cores resulting from low mantle densities require more core Fe to fill up to their mass fraction so less Fe stays behind in the mantle. This means the $\left(\frac{\chi_{FeO}^{sil}}{\chi_{Fe}^{met}}\right)$ parameter is low which leads to relatively low $D_{Ni}^{met-sil}$ values (Equation 5). The lowest mantle densities have $D_{Ni}^{met-sil}$ of <1.

Conversely, the higher mantle densities, attained only by mesosiderites, have $D_{Ni}^{met-sil}$ nearing 50. Typical values across all model scenarios are more than 5.

The reverse is true for C partitioning, where a higher $\left(\frac{\chi_{FeO}^{sil}}{\chi_{Fe}^{met}}\right)$ parameter results in a lower partition coefficient (Equation 2). This results in very low partition coefficients for the mesosiderite model scenarios, which support the highest of the mantle densities. The used mesosiderite composition (Jorritsma & van Westrenen, 2025) has no appreciable C; therefore, partitioning of C is irrelevant for the mesosiderite model scenarios. For the H- and EH-chondrites, the lowest calculated value for $D_{C}^{met-sil}$ is 68, meaning that almost all C partitions to the core.

The partitioning of P is more strongly dependent on $\left(\frac{\chi_{FeO}^{sil}}{\chi_{Fe}^{met}}\right)$ (Equation 1) than the partitioning of C (Equation 2). On the lower mantle density limit, where there almost all Fe is required in the core, $\left(\frac{\chi_{FeO}^{sil}}{\chi_{Fe}^{met}}\right)$ is low which results in high partition coefficients (>20). With mantle densities above this limit, partition coefficients diminish rapidly. In this mantle density range, a second control on partitioning behavior comes from the $\ln\left(1-\chi_{S}^{met}\right)$ term. With increasing mantle density and thus lower Fe content, χ_{S}^{met} increases which lowers the P partition coefficient. H- and EH-chondrite model scenarios produce the highest S content core, which results in P partition coefficients as low as 0.08. Mesosiderite model scenarios have a limit of 1.45 due to lower core S content.

Calculated log $K_{app}^{met-sil}Si^{4+}$ values do not exceed 8.9×10^{-8} across all meteorites, resulting in a maximum core molar fraction of 2.2×10^{-4} for Si. This amount does not significantly impact the results.

Maximum values for $D_{O}^{met-sil}$ are 7.5×10^{-4} and corresponding molar fraction of 2.5×10^{-3}. This is a small amount but not insignificant; the solubility of O in Fe is very low, ranging from 0.16 wt% at 1820 K to 2 wt% at 2319 K at atmospheric pressures (Steinberg et al., 1998). The cooling planetesimal exhibits the lower end of this temperature range, so 0.2 wt% O is used for the inner core eutectic composition. This means that a small amount of FeO can use a lot of the Fe in the core for its eutectic composition, limiting the outer core thickness in some model scenarios.

3.2. Core Compositions

Figure 4 summarizes the elemental mass fractions and alloy molar fractions of all model Psyche cores based on mesosiderite (Figure 4ab), ordinary chondrite (Figure 4cd) and enstatite chondrite (Figure 4ef) bulk compositions. The core compositions are nearly identical for each porosity combination with a single mantle density. Adding mantle porosity increases Psyche's grain density and therefore requires a more mass loss by mantle stripping (Equation 14). The original body therefore had a larger size for higher porosities. This increases the CMB pressures for those scenarios. This increased pressure does not significantly affect the partitioning behavior of light elements; however, partition coefficients are barely affected by pressures in this range (Equations 1–8). Since the original body has the same composition regardless of size, this results in nearly identical core compositions, core densities and core volume fractions in the mass balance equation (Equation 10). The only differences between the porosity combinations with a given mantle density are the original volume and corresponding core size, grain density and required mass loss.

Different mantle densities produce different core compositions as they result in different core mass fractions in the mass-balance equation. As such, core compositions are reported per mantle density (Figure 4). The abundance of light elements in the core does not change significantly between the mantle densities (except for P, Section 3.1) but the total core mass, and thus Fe required to fill out the core mass, does. Lower mantle densities are paired with more massive cores and thus, lower light element mass fractions.

3.3. Penetration Ratio

The core has the same axial ratios as the full body. The thickness of the outer core and the thickness of the mantle are also scaled to the same axial ratios. The excess pressure on each axis is therefore scaled to the axis length ratio with the longest axis. The excess pressure is highest on the *a*-axis and lowest on the *c*-axis. However, since the mantle thickness on each axis is scaled to the same ratios, the scaled excess pressure results in an equal penetration ratio over the entire body.

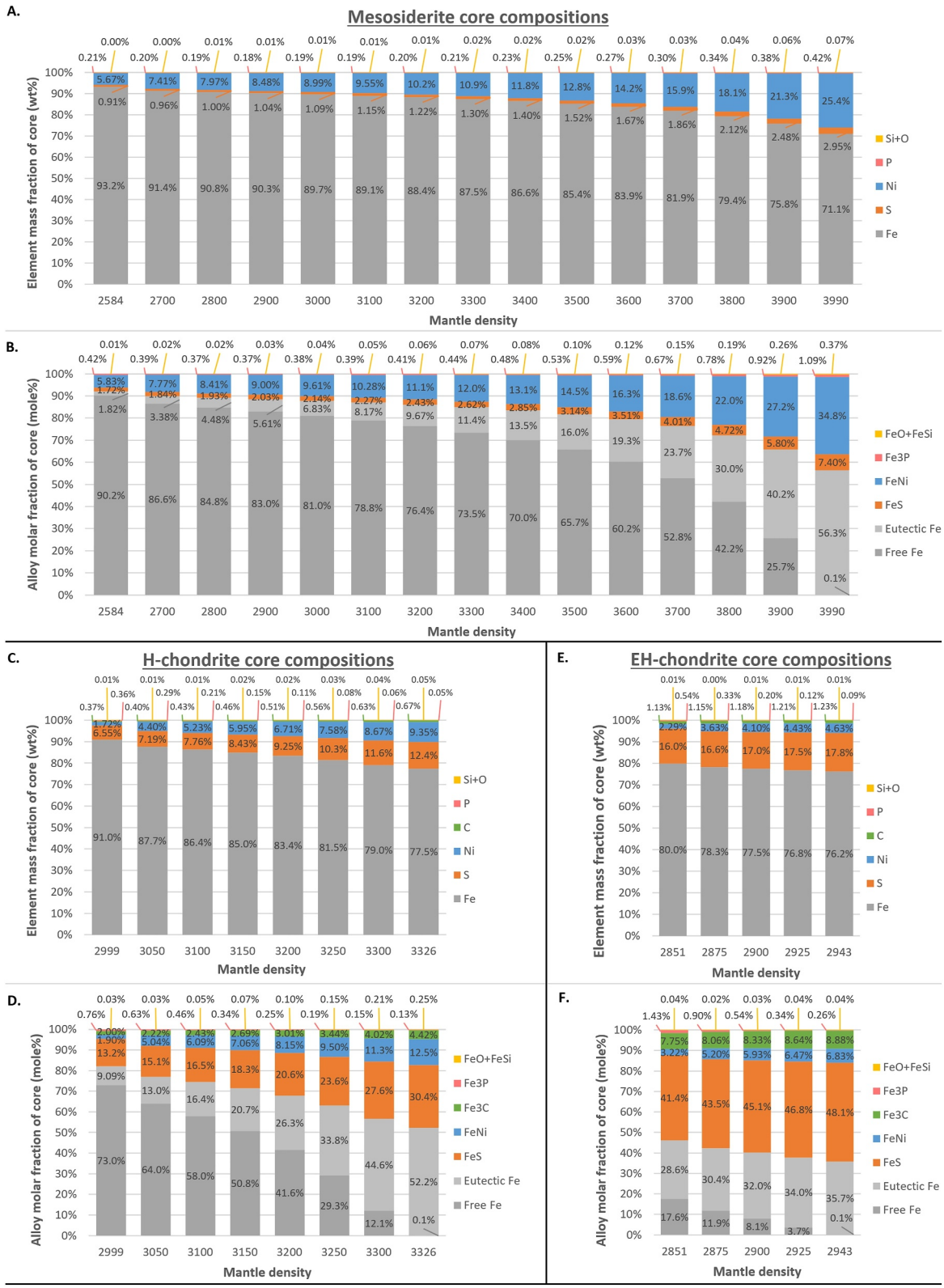

Figure 4. Core compositions in elemental mass fractions and alloy molar fractions for Mesosiderite (a, b), H-Chondrite (c, d) and EH-Chondrite (e, f) models.

The pressure on the *a*-axis is reported in order to assess whether sufficient pressure is generated to overcome the yield strength of the outer core and the mantle. The higher pressure on the *a*-axis means that sufficient pressure to overcome the outer core and mantle yield strengths is attained on this axis first, potentially resulting in a preferential orientation of melt propagation along this axis.

3.4. Mesosiderite Results

The mesosiderite composition has a grain density of 4,400 kg/m^3, above Psyche's bulk density of 4,150 kg/m^3. Therefore, the mantle requires a minimum 7.5%–10% porosity, depending on the mantle density (Figure 5), for Psyche's grain density to be above the meteorite grain density (Section 2.6).

The high meteorite grain density correlates with a high Fe abundance in the used composition (59.4 wt%, Jorritsma & van Westrenen, 2025). This abundance of Fe means that a wide range of mantle densities produces cores within the core size constraints (Section 2.6); on the lower limit of mantle densities (2,584 kg/m^3), the large core mass fraction requires a high amount of Fe. The upper limit of mantle density is constrained by the light element alloys taking up Fe for their eutectic compositions. The abundances of the light elements are comparatively low as a result of the large amount of Fe in the mesosiderite bulk composition. This results in lower core mass fractions for these elements and a high maximum mantle density (3,990 kg/m^3) is possible as a result (Figures 4a and 4b).

Most tested scenarios do not require significant amounts of mass loss (Figure 5a) as the required porosity puts Psyche's grain density just above the mesosiderite grain density. The upper end of the mantle density range does result in small core mass fractions and therefore high mantle thicknesses (Figure 5b). The small cores come at the cost of Fe required to fill out the core mass as the absolute amounts of the minor elements considered are mostly fixed by the extreme partition coefficients. The lowered amount of Fe required to fill out the core increases the relative abundance of these light elements and the portion of Fe they use for eutectic compositions. For the higher mantle densities, this means that there is little Fe available for outer core solidification. Since Ni has to have the same concentration in the outer core and the inner core (Section 2.5), very little FeNi solidifies in the outer core as well. Very little excess pressure and very low penetration ratios are produced as a result (Figure 5cd).

The mantle densities ranging from 2,584–3,800 kg/m^3 do not have these issues. This mantle density range produces reasonably large cores without thick mantles. Excess pressures on the *a*-axis approach or exceed the <10 MPa yield strength for warm iron used by Johnson et al. (2020). The high excess pressures combined with low to medium mantle thicknesses produce a sufficient penetration ratio for almost all scenarios in this mantle density range (Figure 5d), making the mesosiderite bulk composition a suitable candidate for producing ferrovolcanism on Psyche. The mantle density range that produces ferrovolcanism is wide. The minimum porosity requirement can realistically be achieved. The mass loss for most of these scenarios does not exceed 25%.

3.5. H-Chondrite Results

The H-chondrite has a grain density of 3,640 kg/m^3 (Britt & Consolmagno, 2003). This is lower than Psyche's grain density, so no minimum porosity is required. The H-chondrite has the lowest Fe abundance among the bulk compositions of the tested meteorites (27.5 wt%), as well as low amounts of S (2.0 wt%). With Fe and S being the largest contributors to core compositions (Figure 4c), their low abundances result in small maximum core mass fractions, limiting the low-end of mantle densities. Low light element abundances require small amounts of Fe for eutectic compositions, increasing the upper limit on mantle density. This increased density does mean that very high mass loss amounts are required, especially combined with high porosity scenarios (Figure 6a), as these factors increase the grain density gap between Psyche and the meteorite (Section 2.6).

Lower porosities correlate with higher mantle thicknesses that need to be traversed to lead to ferrovolcanism (Figure 6b). However, as adding porosity to the mantle increases the negative buoyancy of Fe + FeS melt in the mantle, lower porosities still produce higher penetration ratios (Figure 7d). High mantle densities leave little free Fe for outer core solidification, resulting in insufficient excess pressures to overcome the yield strengths of the outer core and the mantle (Figure 6c). Lower mantle densities approach the suggested <10 MPa limit to overcome these yield strengths. If these are overcome, ferrovolcanism may be achieved in a narrow range of mantle densities of 2,999–3,100 kg/m^3 (Figure 6d).

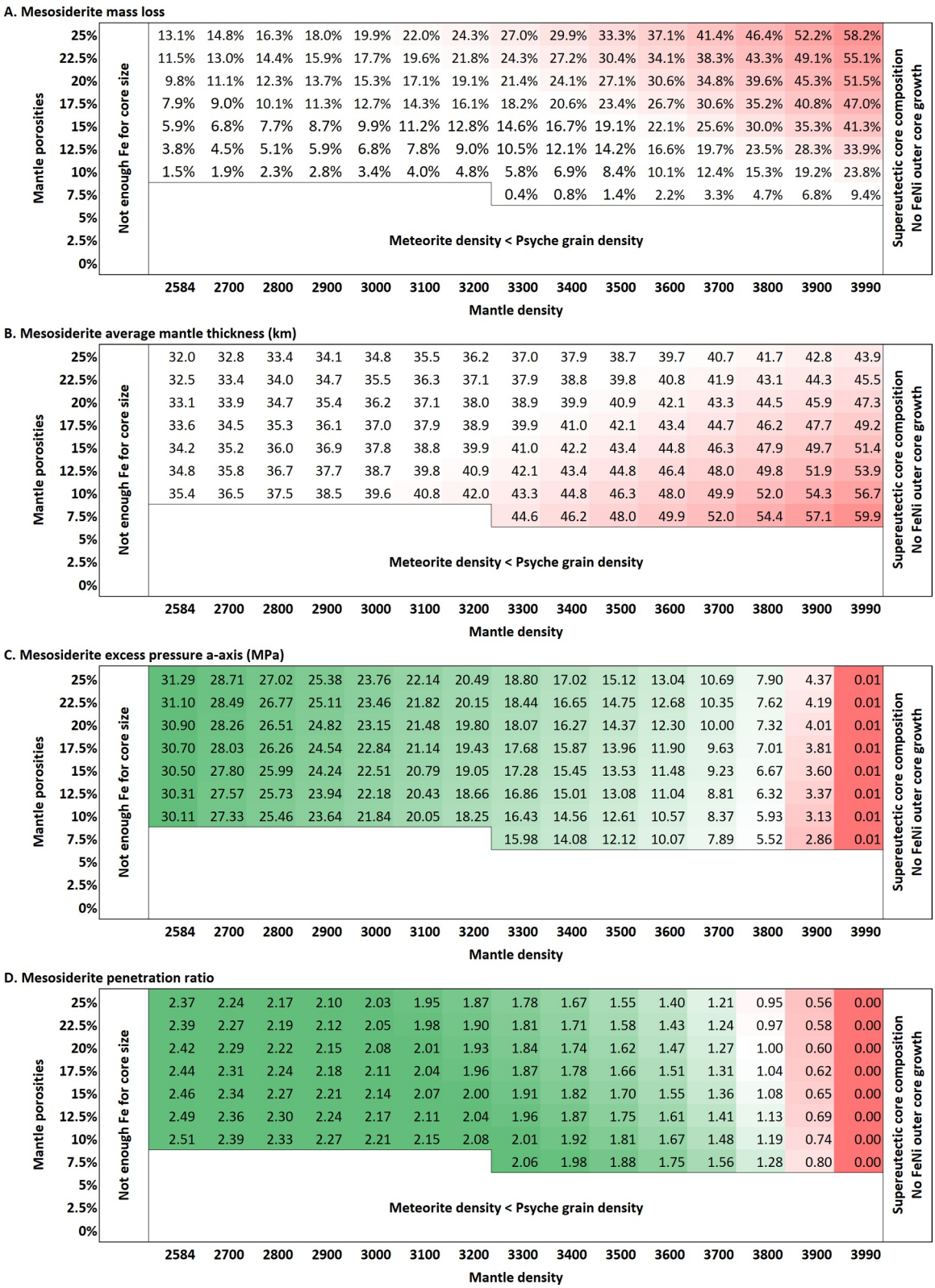

Figure 5. Mesosiderite results for mass loss calculations (a), average mantle thickness (b), excess pressure generated on the *a*-axis (c) and resulting penetration ratios (d) for different mantle density and mantle porosity combinations. Red colors indicate unrealistic mass loss requirements (a), high mantle thickness (b), excess pressures below the yield strength of the outer core (c) and penetration ratios <1 (d) which limit ferrovolcanism possibilities, whereas green colors indicate sufficient excess pressure to overcome the yield strength of the outer core (c) and penetration ratios more than 1 (d).

Adding solid Fe + FeS to the outer core significantly increases the excess pressure and penetration ratios (Figure 7ab). Sufficient pressures to overcome the yield strength of the outer core and mantle are achieved by this mechanism. This helps model scenarios up to 3,200 kg/m^3 produce ferrovolcanism. Scenarios with a 3,250 kg/m^3 mantle and porosities up to 10% also achieve penetration ratios of >1, but pressures generated in these scenarios may not be able to overcome the yield strength of the outer core. Higher mantle densities are associated with a further increased mass loss requirement.

3.6. EH-Chondrite Results

The EH-chondrite composition has a similar Fe abundance (29 wt%) and grain density (3,670 kg/m^3) to the H-chondrite but higher abundances of the highly partitioning light elements (5.8 wt% S and 0.4 wt% C). These almost complete partition to the core (Section 3.1). This means that larger cores are possible with lower mantle densities, as the large cores can be made with less Fe. The lower mantle densities require less mass loss compared to the mantle density range that is viable for the H-chondrite (compare Figures 6a and 6e).

The increased light element abundance in the core also means; however, that almost all of the Fe is required for eutectic compositions in the inner core, and the upper limit of mantle density is significantly diminished as a result (Figure 6f). The possible mantle density range for this meteorite is very narrow (2,851–2,943 kg/m^3).

The low Fe availability for outer core solidification results in insufficient excess pressure to overcome the yield strength of the outer core (Figure 4g) as well as low penetration heights in the mantle, should a melt migration path exist. This leaves the penetration ratio very low for all scenarios (Figure 4h).

Adding Fe + FeS to the solid outer core increases the column height but significantly decreases the outer core density as there is little Fe and FeNi to contribute to the average outer core density. The average density is dominated by the density of the added eutectic Fe + FeS, which is significantly lower. The excess pressure is increased to sufficient levels to possibly overcome the yield strength of the outer core and mantle (Figure 7c). A very limited number of model scenarios at the lower density limit generate sufficient penetration ratios (Figure 7d).

3.7. Results Overview

The mesosiderite bulk composition readily produces ferrovolcanism in a wide range of model scenarios with a mantle density between 2,584 and 3,800 kg/m^3 without requiring excessive mass loss. A minimum 7.5%–10% mantle porosity is required. Overall, from a chemical perspective, this composition is most likely to produce ferrovolcanism.

H-chondrite model scenarios produce ferrovolcanism in a narrow but not unrealistic mantle density range of 2,999–3,100 kg/m^3. Large amounts of mass loss are required for these scenarios. Additional solidification of Fe + FeS extends the mantle density range that produces ferrovolcanism up to 3,200 kg/m^3. This mechanism yields a limited available melt volume. The increased mantle densities that produce ferrovolcanism have even higher mass loss requirements.

The EH-chondrite model scenarios have tight mantle density limits due to the low Fe and high light element abundances in the core. The high light element abundances further limit outer core growth, making it unlikely to produce ferrovolcanism. Additional outer core growth has to be considered for a very limited number of model scenarios to achieve penetration ratios of more than 1. The possibility for this meteorite to produce an FeNi outer core, as well as subsequent ferrovolcanism, is minimal.

4. Discussion

4.1. Sensitivity to Input Parameters

The model uses simplified physical parameters for Psyche.

A bulk density of 4,150 kg/m^3 was used throughout. The most recent mass and volume estimates combine for a bulk density of 4,187 (−240/+86) kg/m^3. As discussed in Section 3.2, different porosities do not produce different core compositions but only different core sizes and mass loss requirements. The core mass fraction and core composition of the original body depend only on the mantle density. The same is true for the bulk density; a

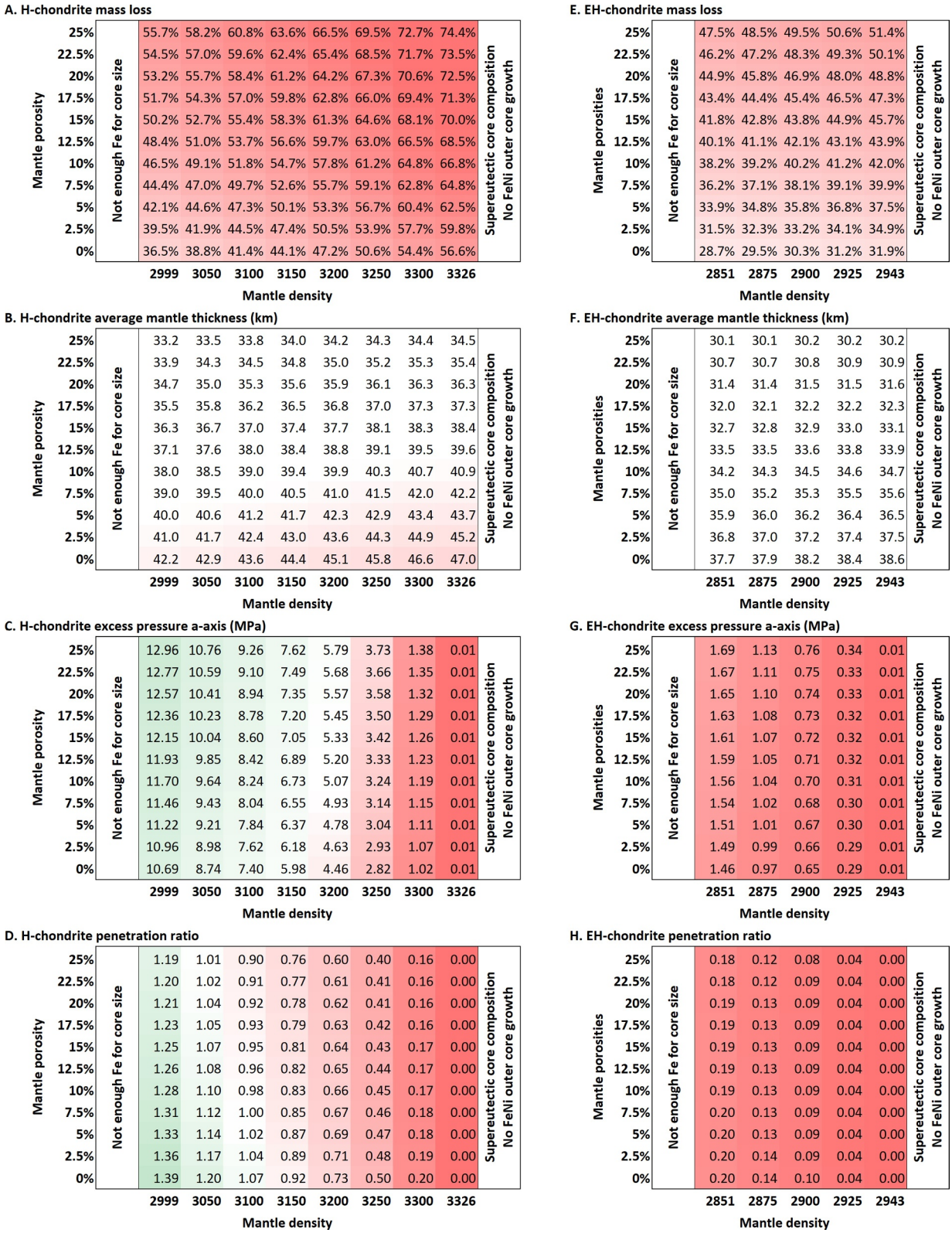

Figure 6. H-chondrite and EH-chondrite results for mass loss calculations (a, e), average mantle thickness (b, f), excess pressure generated on the *a*-axis (c, g) and resulting penetration ratios (d, h) for different mantle density and mantle porosity combinations. Red colors indicate unrealistic mass loss requirements (a, e), high mantle thickness (b, f), excess pressures below the yield strength of the outer core (c, g) and penetration ratios <1 (d, h) which limit ferrovolcanism possibilities, whereas green colors indicate sufficient excess pressure to overcome the yield strength of the outer core (c, g) and penetration ratios >1 (d, h).

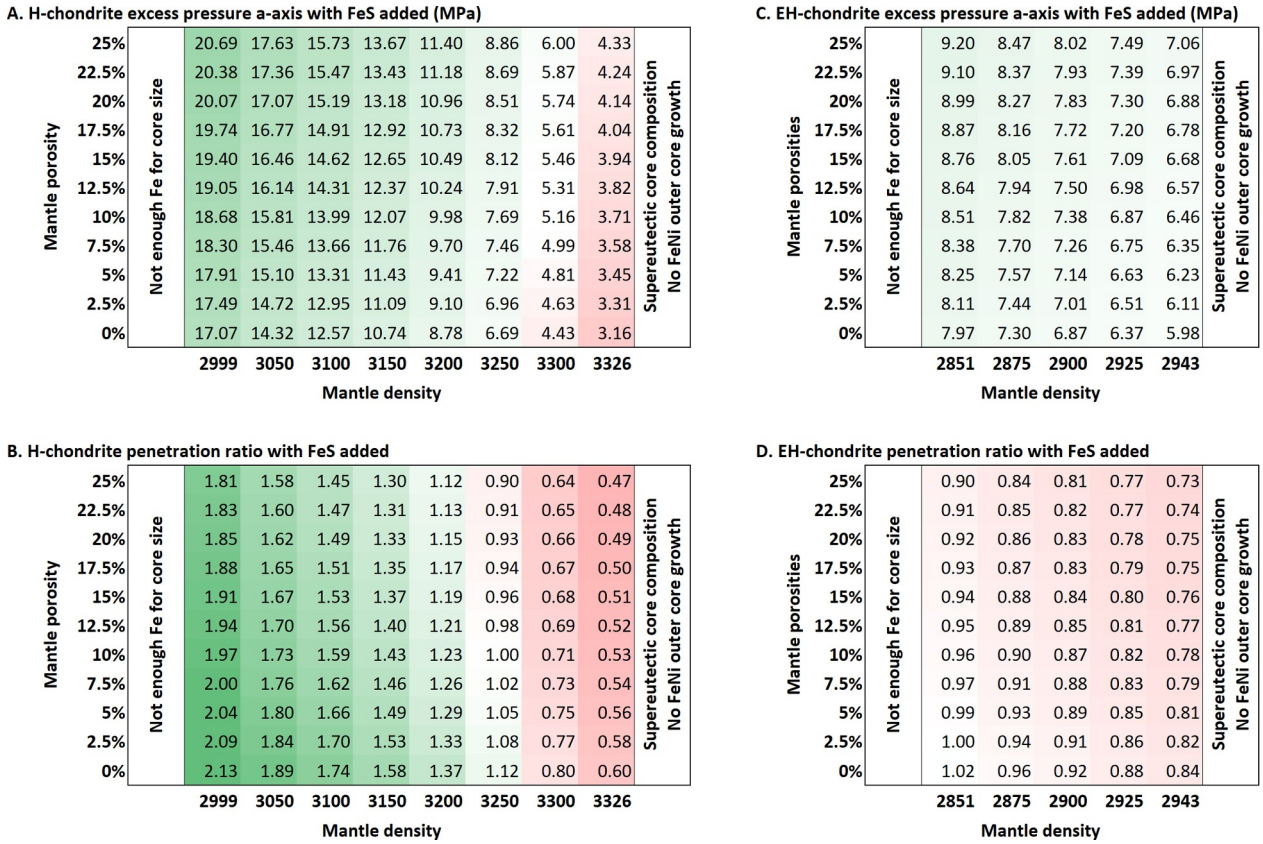

Figure 7. Excess pressure on the *a*-axis and penetration ratio for H-chondrite (a, b) and EH-chondrite (c, d) scenarios after solidifying 90 mol% of the eutectic Fe + FeS layer. Red colors indicate excess pressures below the yield strength of the outer core (a, c) and penetration ratios <1 (b, d), which limit ferrovolcanism possibilities, whereas green colors indicate sufficient excess pressure to overcome the yield strength of the outer core (a, c) and penetration ratios >1 (b, d).

higher bulk density, similar to a higher mantle porosity, requires a larger core size in the mass balance equation (Equation 10), which is produced in a larger original body. The CMB pressure in this body does not sufficiently increase to be significant in the metal-silicate partitioning equations. The larger original body therefore has the same core composition, density and original volume fraction. The mantle density limits remain the same. The increased size of the original body is compensated for by an increased mass loss. For mesosiderite scenarios, this also lowers the mantle porosity requirements. The larger core produces a thicker outer core and comes with a thinner mantle, both of which increase the penetration ratio for all model scenarios. A higher bulk density is therefore more likely to produce ferrovolcanism.

Conversely, using a lower bulk density decreases the core mass in the mass balance equation, which results in a smaller core from a smaller original body. This produces a thinner outer core and a thicker mantle, decreasing the penetration ratio for all model scenarios. This is not conducive to producing ferrovolcanism. The minimum porosity requirement for mesosiderite model scenarios is increased and the mass loss requirements for all model scenarios are decreased.

The shape model is simplified to a perfect tri-axial ellipsoid to make volume and thickness calculations of different layers possible. The core is assigned the same axial ratio as the full body. This gives the body an equal mass distribution which is in line with the theory by Ferrais et al. (2020) that Psyche's ellipsoidal shape is a remnant of a Jacobi-ellipsoid. However, the shape may also be caused by asymmetric mass loss, decreasing the *c*-axis length from an originally spherical shape. In this case, the core may be spherical.

A spherical core increases the potential column height on the *c*-axis while decreasing the mantle thickness, thereby increasing the penetration ratio on the *c*-axis. The opposite is true for the *a*-axis. Thus, the possibility for ferrovolcanism to occur increases on the *c*-axis while it decreases on the *a*-axis. The excess pressure is equalized

over the entire core instead of being scaled to the major axis ratios. This means that is the excess pressures in this case would be lower than the reported *a*-axis excess pressures (Figures 5–7).

Additionally, the core may not be perfectly centered. Psyche's spin parameters indicate that the center of gravity is located on the *c*-axis, which corresponds to the spin axis (Shepard et al., 2017). However, the center of gravity, highly dependent on the placement of the core, is not necessarily in the center of the spin axis. The core can be situated anywhere along the *c*-axis, producing asymmetrical mantle thicknesses along this axis. This has implications for the possibility of ferrovolcanism as the column height used to calculate excess pressure remains the same but the penetration height required to produce ferrovolcanism changes; one end of the *c*-axis has a thicker mantle that requires more pressure, whereas the opposite end has a thinner mantle that therefore requires less pressure. Haba et al. (2019) suggested that a hit-and-run collision on Vesta with subsequent asymmetrical reaccretion could cause a heterogeneous mantle thickness, a mechanism that fits in the ferrovolcanism framework outlined in this work.

Disc-averaged measurements indicate high radar albedo areas in the southern hemisphere, in correlation with high optical albedo (Shepard et al., 2021). Some craters have been suggested on the southern hemisphere in Psyche's shape model (Shepard et al., 2021 and references therein) although the disc-averaged nature of the measurements means that data resolution is too poor to firmly suggest a correlation. If this correlation exists, it might be caused by a thinner mantle and weakened lithosphere from the impact causing the crater, making dike propagation through the mantle easier underneath the crater floor. Combined with a spherical core, producing higher penetration ratios along the *c*-axis, this might help explain a preferential orientation of ferrovolcanism along this axis. If the core is not centered, with a lower mantle thickness on the southern axis as a result, the southern hemisphere has an increased likelihood of producing ferrovolcanism compared with the northern hemisphere. Alternatively, the impact causing this crater may have excavated previously emplaced ferromagmatic diapirs (Raducan et al., 2020).

Lastly, a spherical non-centered core might make the mantle sufficiently thin for impact cratering to reach the CMB, exposing the core and creating a mixed iron-silicate regolith (Kim & Hirabayashi, 2022). This could also explain the correlation between high radar albedo and cratering in the southern hemisphere, without requiring ferrovolcanism.

4.2. Sensitivity to Partitioning Values

The metal-silicate distribution of Ni, C, O and S during core formation was calculated based on the partitioning equations by Steenstra & van Westrenen (2018). These equations are calibrated for the pressure-temperature range of the Moon (0–5 GPa). The partitioning of P was parameterized based on experiments performed at 1.5 GPa in addition to data previously obtained at <5 GPa (Steenstra et al., 2017). These pressures and the corresponding silicate liquidus temperatures are both significantly higher than those inferred for Psyche in this work and therefore might not be applicable. Extreme partition coefficients are expected at low pressure; however (Bercovici et al., 2022), resulting in most of the considered elements either mostly or barely partitioning into the core. Above a threshold where simply "most" of a particular element partitions into the core, the accuracy of the calculated partition coefficient becomes insignificant as the resulting core composition is not significantly affected. Proper calibration is more important at pressures where the distribution starts to become more equal. This is the case for the partitioning of Ni and P (Section 3.1). Of these, the partitioning of Ni plays a large role as a primary contributor to outer core growth. It does not use eutectic Fe but does use Fe for its alloy. Reducing or increasing the Ni content of the core directly influences the FeNi content of the outer core. With less Ni in the core, more Fe is available for outer core growth which somewhat mitigates the effect on outer core volume and subsequent column height.

Regarding the effect of phosphorous, the EH-chondrite has the highest bulk P content at 0.2 wt%, resulting in a maximum 0.5 wt% P in the core in our models. This uses an additional ~4.5 wt% Fe in its alloy and eutectic composition which is consequently unavailable for outer core growth. P partitions more into the core at lower mantle densities due to the effect of the $\left(\frac{\chi_{FeO}^{sil}}{\chi_{Fe}^{met}}\right)$ parameter (Section 3.1). Regardless, penetration ratios remain higher at lower mantle densities. In most of the model scenarios, P does not readily partition into the core, therefore using a lot less Fe. Other than decreasing the outer core growth by using Fe, the core P content has no effect on the ferrovolcanism mechanism as it separates from the sulfide melt into the inner core.

The reported center values of the partitioning equations and log C_S calculation (Equations 1–6 and 8) are used in the model. The upper and lower error margins were tested for sensitivity. The pressure and temperature were also tested for sensitivity. Although calculated partition coefficients of C, S, Si and O can change by up to ~50%, their overall behavior does not change and resulting core compositions are not significantly affected.

4.3. Meteorite Compositions

The meteoritic bulk compositions used in this work were selected based on a subjective assessment of the likelihood that Psyche may have been built from them. The H- and EH-chondrites were chosen for their undifferentiated nature (Section 2). This nature perfectly fits this work's modeling framework, calculating the core differentiation and light element partitioning from a fully molten undifferentiated state in the early stages of condensation in the solar system. Mesosiderites have a more circumstantial possibility to be a building block for Psyche, although a fully molten state can hypothetically be achieved by a massive impact (Ferrais et al., 2020).

Additional uncertainties arise from the use of meteorite grain densities from Britt and Consolmagno (2003). A meteorite's grain density is highly sensitive to the relative abundances of silicate and metallic parts. This ratio can be particularly variable between smaller meteorite samples. The meteorite grain densities measured by Britt and Consolmagno (2003) were used to calculate Psyche's mass loss, original volume and original core volume fraction and the corresponding pressure at which partitioning occurred. However, these grain densities are not necessarily the same as the grain densities of the meteorite samples that were used for mass spectrometry. The used compositions and grain densities of the meteorites may not correlate.

The H- and EH-chondrite bulk compositions both have comparatively low Fe contents, unable to produce large cores with thin mantles. The low Fe abundance means that there are comparatively more light elements in the bulk composition, of which C and S mostly partition to the core as well as P in some model scenarios. The subsequent highly light element enriched cores use a lot of the available Fe for eutectic compositions, leaving little Fe for outer core growth. The mantle density window for both meteorites is tightly constrained on the lower and high ends by the low Fe abundance (Section 2.6). The EH-chondrite has the highest S, C and P abundances and struggles to produce ferrovolcanism as a result; it has the narrowest mantle density window and the eutectic compositions of the light elements in the inner core leave very little Fe to grow a solid FeNi outer core. Counterintuitively, the most light element enriched cores do not produce ferrovolcanism because of this. Additionally, the chondrites' low Fe fractions are related to a low grain density. Mass loss has to be considered in order to increase a meteorite's grain density to Psyche's grain density. Both chondritic bulk compositional models require significant mass loss amounts to result in a planetesimal with 4,150 kg/m^3 bulk density.

The mesosiderite bulk composition better fits the chemical requirements for producing ferrovolcanism. The high grain density is related to a large Fe fraction which is required for the wide range of mantle densities to fall within core size constraints. However, the conditions for a fully molten state, required in the framework of this model, are more circumstantial than for the undifferentiated chondrites.

The Fe content in the bulk composition is the leading chemical constraint in this model. A higher bulk Fe content naturally comes with a lower abundance in other core forming elements, which is conducive to producing ferrovolcanism. Additionally, a high bulk Fe content is related to a high grain density, which reduces the mass loss requirements to equalize the meteorite and asteroid grain densities. The abundances of S, C and P are a secondary constraint as showcased by the different results for the H- and EH-chondrite model scenarios.

Alternative promising building blocks may be the CH- and CB-chondrites. These are primitive building blocks that therefore naturally fit the ferrovolcanism model, with a high bulk Fe content and putative grain density compared to the H- and EH-chondrites tested in this work. These should be chemically conducive to producing ferrovolcanism as described above, have lower mass loss requirements compared to H- and EH-chondrite model scenarios and forego the main drawback of the mesosiderite composition. Available data on the elemental composition and grain density of these meteorite types are insufficient to test this with our model.

4.4. Core Composition and Density

The core density is calculated based on the ideal mixing of binary systems for each light element, using unit-cell volumes and molar abundances (Section 2.3). Low P/T unit-cell volumes are used for the density calculations in the mass balance as these are readily available. These are accurate for use in the mass balance as they reflect the

current cooled state of the core. The same density is used in the CMB-pressure calculations, which is inaccurate, as the core and mantle had not solidified at the time of partitioning that the pressure is calculated for. Considering thermal expansion for this step would not significantly impact results, the resulting pressure would still be too low to significantly impact partition coefficients, resulting in very similar core compositions.

A thermal expansion factor was used to calculate the excess pressure generated when the core was not fully cooled, to correct for the difference between low and high temperature unit-cell volumes. This correction is highly simplified. The corrected volumes are only used to calculate a more accurate density contrast in excess pressure calculations, and the outer core volume and thickness over a molten inner core with a larger volume than its cooled equivalent (Figure 3).

A maximum mantle density is obtained when all of the available Fe is used in eutectic compositions of light elements. This is again done using an ideal mixing approach where each light element has its own binary eutectic Fe requirement. The fully integrated multicomponent mixing behavior of all the considered light elements is poorly understood. Mixing of light element systems may require less eutectic Fe than when treating them individually. This would increase the maximum mantle density as this is constrained by the amount of Fe required for eutectic compositions. This effect is mitigated by the formation of immiscible liquids as this separates the Fe-S system from the other light elements. The Fe-S system requires its own eutectic Fe in this scenario. The overlap in eutectic Fe should then only be considered in the inner core.

The formation of immiscible liquids is central to the model and strongly supported by experimental data (e.g., Dasgupta et al. ,2009; Hakim et al., 2019; Bercovici et al., 2022, Bromiley et al., 2024 and references therein). If no immiscible liquids are produced in the inner core, the melt density increases and excess pressures across all scenarios are thereby decreased, resulting in a lower likelihood for ferrovolcanism to occur.

4.5. Mass Loss

Bonsor et al. (2015) performed *N*-body simulations of impacts between two bodies of >0.16 Earth masses with varying mass ratios and impact parameters, to model the accretion of protoplanets from smaller differentiated planetesimals. They show that around 30% of collisions between planetesimals of this size result in near perfect mergers, whereas only 10% of impacts result in any amount of mass loss. This means that significant mass loss over the collision history of larger planetesimals is unlikely. A sequence of erosional collisions is likely required for higher mass loss amounts, as most individual erosional impacts result in a smaller amount of mass loss. However, for smaller differentiated planetesimals in the early phases of solar system accretion, hit-and-run collisions with larger amounts of preferential erosion of the mantle have been suggested (e.g., Asphaug & Reufer, 2014; Asphaug et al., 2006; Carter et al., 2018; O'Neill & Palme, 2008). Cambioni et al. (2021) suggest that hit-and-run collisions are far more likely between planetesimals of <0.1 Earth mass, with perfect merger collisions becoming dominant above this threshold. Such erosive impacts have been suggested to be at the origin of Psyche's comparatively high bulk density (Cambioni et al., 2024, 2025). Similarly, a giant impact with mantle stripping has been proposed by Ferrais et al. (2020), which allows for non-primitive meteorites to be considered as building blocks (Section 2). This type of erosion is most likely to have occurred during the early stages of solar system evolution, which is consistent with the timeframe at which molten metal was still present in Psyche's core.

A limited amount of mass loss is required to form Psyche from a mesosiderite composition. It should be noted; however, that a lot of initial mass loss is implied in the giant impact that hypothetically left a remnant Psyche with a mesosiderite composition (Ferrais et al., 2020).

The H- and EH-chondrites, which have lower grain densities, require significant amounts of mass loss of the mantle to increase the original grain density to Psyche's current grain density. One or more hit-and-run collisions or giant impacts as the final steps of accretion may have caused these mass loss amounts, similar to the giant impact proposed as the reason for Psyche's potential mesosiderite bulk composition.

Preferential stripping of mantle material is highly conducive to producing ferrovolcanism. The decreased mantle volume fraction is paired with an increased core volume fraction. The larger core can produce more excess pressure and the decreased mantle thickness is easier to overcome with that pressure, resulting in higher penetration ratios.

4.6. Outer Core Growth

The ferrovolcanism mechanism relies on having the core solidifying from the outside in. The initialization of core growth at the outer core may not be uncommon for low pressure planetesimals as the core adiabat is steeper than the core liquidus (Williams, 2009). The extent that outer core growth can continue is uncertain, as a dense solid outer core is gravitationally unstable. Instead of growing inward, solids nucleating at the CMB might sink and accumulate in the center (e.g., Neufeld et al., 2019; Nichols-Fleming et al., 2024).

Johnson et al. (2020) consider a dendritic outer core growth trapping melt in the interdendritic space. These melt pockets are the proposed source of ferrovolcanism. The available melt volume is however unexplored. This work's model uses concentric outer core growth, using the inner core as the melt reservoir. Scheinberg et al. (2016) modeled core solidification on a 200-km core with a 1-km mantle and concluded that concentric outer core growth is unlikely. Instead, the dendritic outer core growth is preferred. Instead of considering ferrovolcanism, the model by Scheinberg et al. (2016) assumed that the trapped melt solidifies in situ.

As discussed in Sections 3.5 and 3.6, adding concentric solid eutectic Fe + FeS to the outer core increases the penetration ratios and helps the H-chondrite produce ferrovolcanism in a wider range of model scenarios. This should be the case whether Fe + FeS is solidified as a concentric layer after the solidification of the FeNi outer core, as described in this work, or in interdendritic space as suggested by Scheinberg et al. (2016). This may serve as a hybrid between this work's model and the work by Johnson et al. (2020), where the outer core grows in dendrites but the inner core is used as a melt reservoir. Again, the penalty to available melt volume should be considered, as very small molten sulfide volumes remain in this framework. The fraction of a melt reservoir that can be expelled if sufficient pressure is achieved has not been explored.

5. Conclusions

Sufficient penetration ratios are produced in some scenarios if the boundary conditions for the ferrovolcanism mechanism are met; in these cases, progressive concentric outer core solidification is required.

The model outcomes are very sensitive to Psyche's bulk density as this dictates the core and mantle volume fractions. Mass loss is required in the model framework as a way to reconcile input meteorite density and Psyche's grain density, especially for the H- and EH-chondrites. This struggle to produce a body with high grain density while satisfying compositional constraints in the core. The range of mantle densities that falls within core size constraints is very narrow but does exhibit a common range for mantle densities in the solar system.

This behavior is largely dictated by Fe abundance in the bulk composition. High Fe amounts are required to produce significant outer core thicknesses after the eutectic compositions of the light elements in the inner core are satisfied. High Fe abundances correlate to higher grain densities, which result in lower mass loss requirements, as well as increasing the viable mantle density range that falls within chemical and mass balance constraints.

The mesosiderite bulk composition more readily produces ferrovolcanism, over a far wider mantle density range, due to the high abundance of Fe. High grain density means that little mass loss is required, instead requiring minimum 7.5%–10% mantle porosities to produce a planetesimal with equal grain density. Mesosiderite is not a primitive building block; however and therefore, does not naturally fit the methodology outlined in this work. The chondrites fit better in the ferrovolcanism framework but are otherwise limited in being able to produce ferrovolcanism.

All of the tested model scenarios require significant mass loss amounts; the H- and EH-chondrites explicitly to achieve Psyche's grain density, and the mesosiderite implicitly through the idea that Psyche is a mesosiderite-like remnant of a giant impact in an initially much larger body (Ferrais et al., 2020). Mantle stripping by hit-and-run collisions or giant impacts is highly conducive to producing ferrovolcanism and fits the timing of the ferrovolcanism framework; both are tied to the early phases of solar system accretion.

Ferrovolcanism is itself quite a novel and relatively unexplored phenomenon. The poorly understood core solidification and melt dynamics in this framework make it hard to rule out. With the uncertain boundary conditions, the low possibility for the chondrites to produce ferrovolcanism and the circumstantial possibility for mesosiderites to fit the ferrovolcanism framework tested in this work, the only conclusion to be made is that ferrovolcanism is possible, not that it is likely or even probable. Other, perhaps simpler and more intuitive mechanisms could also provide the origin for Psyche's enigmatic appearance and should similarly be considered.

The low data resolution of Psyche's surface properties provides few stringent tests with which to corroborate or disprove the ferrovolcanism theory. With NASA's Psyche mission set to arrive at the asteroid at the end of this decade, this data set is sure to improve. These data will be the true test for the ferrovolcanism hypothesis. The mission will include gravity and magnetometry investigations (Weiss et al., 2023; Zuber et al., 2022). Measurements of the moment of inertia can be used to assess whether Psyche is a differentiated planetesimal, what the core size, shape, placement and mantle thicknesses are, and whether the core grew concentrically inward or not (Nichols-Fleming et al., 2024). Additionally, ferrovolcanic dykes or provinces may have detectable magnetic signatures from a dynamo generated in a solidifying core (Courville et al., 2025). Together with models such as the ones developed here, these investigations will further constrain whether ferrovolcanism is the origin for Psyche's surface characteristics.

Conflict of Interest

The authors declare no conflicts of interest relevant to this study.

Data Availability Statement

All calculations were done in an Excel-based model exclusively using cell references (no macros). The Excel file used for model calculations in this study is available at Mendeley Data via https://doi.org/10.17632/sbdxrws596.1. *Jorritsma and van Westrenen (2025).

Acknowledgments
We would like to thank Jurrien Knibbe in particular for his advice on the calculation of core densities.

References

Abrahams, J. N. H., & Nimmo, F. (2019). Ferrovolcanism: Iron volcanism on metallic asteroids. *Geophysical Research Letters*, *46*(10), 5055–5064. https://doi.org/10.1029/2019GL082542

Asphaug, E., Agnor, C. B., & Williams, Q. (2006). Hit-and-run planetary collisions. In *Nature*, (Vol. 439(7073), pp. 155–160). Nature Publishing Group. https://doi.org/10.1038/nature04311

Asphaug, E., & Reufer, A. (2014). Mercury and other iron-rich planetary bodies as relics of inefficient accretion. *Nature Geoscience*, *7*(8), 564–568. https://doi.org/10.1038/ngeo2189

Becker, T. M., Cunningham, N., Molyneux, P., Roth, L., Feaga, L. M., Retherford, K. D., et al. (2020). HST UV observations of asteroid (16) psyche. *The Planetary Science Journal*, *1*(3), 53. https://doi.org/10.3847/PSJ/abb67e

Bercovici, H. L., Elkins-Tanton, L. T., O'Rourke, J. G., & Schaefer, L. (2022). The effects of bulk composition on planetesimal core sulfur content and size. *Icarus*, *380*, 114976. https://doi.org/10.1016/j.icarus.2022.114976

Binzel, R. P., Bus, S. J., Xu, S., Sunshine, J., Burbine, T. H., Neely, A. W., & Brown, R. W. (1995). Rotationally resolved spectra of asteroid 16 psyche. *Icarus*, *117*(2), 443–445. https://doi.org/10.1006/icar.1995.1170

Bonsor, A., Leinhardt, Z. M., Carter, P. J., Elliott, T., Walter, M. J., & Stewart, S. T. (2015). A collisional origin to Earth's non-chondritic composition? *Icarus*, *247*, 291–300. https://doi.org/10.1016/j.icarus.2014.10.019

Bouvier, A., Blichert-Toft, J., Moynier, F., Vervoort, J. D., & Albarède, F. (2007). Pb–Pb dating constraints on the accretion and cooling history of chondrites. *Geochimica et Cosmochimica Acta*, *71*(6), 1583–1604. https://doi.org/10.1016/j.gca.2006.12.005

Breuer, D., Rueckriemen, T., & Spohn, T. (2015). Iron snow, crystal floats, and inner-core growth: Modes of core solidification and implications for dynamos in terrestrial planets and moons. *Progress in Earth and Planetary Science*, *2*(1), 39. https://doi.org/10.1186/s40645-015-0069-y

Britt, D. T., & Consolmagno, G. J. S. J. (2003). Stony meteorite porosities and densities: A review of the data through 2001. *Meteoritics & Planetary Sciences*, *38*(8), 1161–1180. https://doi.org/10.1111/j.1945-5100.2003.tb00305.x

Bromiley, G. D., Varnam, M., Terasaki, H., Komabayashi, T., & Barosch, J. (2024). The extent of liquid immiscibility in planetesimal cores. *Geochemical Perspectives Letters*, *33*, 7–12. https://doi.org/10.7185/geochemlet.2445

Bryson, J. F. J., Nichols, C. I. O., Herrero-Albillos, J., Kronast, F., Kasama, T., Alimadadi, H., et al. (2015). Long-lived magnetism from solidification-driven convection on the pallasite parent body. *Nature*, *517*(7535), 472–475. https://doi.org/10.1038/nature14114

Cambioni, S., de Kleer, K., & Shepard, M. (2022). The heterogeneous surface of asteroid (16) psyche. *Journal of Geophysical Research: Planets*, *127*(6), e2021JE007091. https://doi.org/10.1029/2021JE007091

Cambioni, S., Jacobson, S. A., Emsenhuber, A., Asphaug, E., Rubie, D. C., Gabriel, T. S. J., et al. (2021). The effect of inefficient accretion on planetary differentiation. *Planetary Science Journal*, *2*(3), 93. https://doi.org/10.3847/PSJ/abf0ad

Cambioni, S., Weiss, B. P., Asphaug, E., Baijal, N., Biersteker, J. B., Bottke, W. F., et al. (2025). Formation of asteroid (16) psyche by a giant impact. In *56th lunar and planetary science conference, the woodlands, Texas, United States*. Retrieved from https://www.hou.usra.edu/meetings/lpsc2025/pdf/1317.pdf

Cambioni, S., Weiss, B. P., Asphaug, E., Volk, K., Emsenhuber, A., Biersteker, J. B., et al. (2024). Can metal-rich worlds form by giant impacts? Retrieved from https://arxiv.org/abs/2408.15340

Cantillo, D. C., Reddy, V., Sharkey, B. N. L., Pearson, N. A., Sanchez, J. A., Izawa, M. R. M., et al. (2021). Constraining the regolith composition of asteroid (16) psyche via laboratory visible near-infrared spectroscopy. *The Planetary Science Journal*, *2*(3), 95. https://doi.org/10.3847/PSJ/abf63b

Carry, B. (2012). Density of asteroids. *Planetary and Space Science*, *73*(1), 98–118. https://doi.org/10.1016/j.pss.2012.03.009

Carter, P. J., Leinhardt, Z. M., Elliott, T., Stewart, S. T., & Walter, M. J. (2018). Collisional stripping of planetary crusts. *Earth and Planetary Science Letters*, *484*, 276–286. https://doi.org/10.1016/j.epsl.2017.12.012

Chambers, J. E. (2013). Late-stage planetary accretion including hit-and-run collisions and fragmentation. *Icarus*, *224*(1), 43–56. https://doi.org/10.1016/j.icarus.2013.02.015

Chopelas, A., & Boehler, R. (1992). Thermal expansivity in the lower mantle. *Geophysical Research Letters*, *19*(19), 1983–1986. https://doi.org/10.1029/92GL02144

Cloutis, E. A., Hardersen, P. S., Reddy, V., Gaffey, M. J., Bailey, D. T., & Craig, M. A. (2009). Metal-orthopyroxene and metal-olivine mixtures: Spectral reflectance properties and implications for asteroid spectroscopy. In *40th lunar and planetary science conference*. abstract #1332.

Coradini, A., Capaccioni, F., Erard, S., Arnold, G., De Sanctis, M. C., Filacchione, G., et al. (2011). The surface composition and temperature of asteroid 21 lutetia as observed by Rosetta/VIRTIS. *Science*, *334*(6055), 492–494. https://doi.org/10.1126/science.1204062

Courville, S. W., Sanderson, H., Bierson, C. J., Elkins-Tanton, L. T., Oran, R., O'Rourke, J. G., et al. (2025). *Ferrovolcanic intrusions on asteroid (16) psyche May be magnetized*. ESS Open Archive. https://doi.org/10.22541/essoar.174164188.87804085/v1

Dasgupta, R., Buono, A., Whelan, G., & Walker, D. (2009). High-pressure melting relations in fe–c–s systems: Implications for formation, evolution, and structure of metallic cores in planetary bodies. *Geochimica et Cosmochimica Acta*, *73*(21), 6678–6691. https://doi.org/10.1016/j.gca.2009.08.001

Domingue, D. L., Vilas, F., Holsclaw, G. M., Warell, J., Izenberg, N. R., Murchie, S. L., et al. (2010). Whole-disk spectrophotometric properties of Mercury: Synthesis of MESSENGER and ground-based observations. *Icarus*, *209*(1), 101–124. https://doi.org/10.1016/j.icarus.2010.02.022

Doyle, A. E., Young, E. D., Klein, B., Zuckerman, B., & Schlichting, H. E. (2019). Oxygen fugacities of extrasolar rocks: Evidence for an Earth-like geochemistry of exoplanets. *Science*, *366*(6463), 356–359. https://doi.org/10.1126/science.aax3901

Drummond, J. D., Merline, W. J., Carry, B., Conrad, A., Reddy, V., Tamblyn, P., et al. (2018). The triaxial ellipsoid size, density, and rotational pole of asteroid (16) psyche from Keck and Gemini AO observations 2004–2015. *Icarus*, *305*, 174–185. https://doi.org/10.1016/j.icarus.2018.01.010

Elkins-Tanton, L. T., Asphaug, E., Bell, J. F., Bercovici, H., Bills, B., Binzel, R., et al. (2020). Observations, Meteorites, and models: A preflight assessment of the composition and formation of (16) psyche. In *Journal of geophysical research: Planets*, (Vol. 125(3). e2019JE006296, Blackwell Publishing Ltd. https://doi.org/10.1029/2019JE006296

Farnocchia, D., Fuentes-Muñoz, O., Park, R. S., Baer, J., & Chesley, S. R. (2024). Mass, density, and radius of asteroid (16) psyche from high-precision astrometry. *The Astronomical Journal*, *168*(1), 21. https://doi.org/10.3847/1538-3881/ad50ca

Ferrais, M., Vernazza, P., Jorda, L., Rambaux, N., Hanuš, J., Carry, B., et al. (2020). Asteroid (16) Psyche's primordial shape: A possible Jacobi ellipsoid. *Astronomy and Astrophysics*, *638*, L15. https://doi.org/10.1051/0004-6361/202038100

Fornasier, S., Clark, B. E., Dotto, E., Migliorini, A., Ockert-Bell, M., & Barucci, M. A. (2010). Spectroscopic survey of M-type asteroids. *Icarus*, *210*(2), 655–673. https://doi.org/10.1016/j.icarus.2010.07.001

Haba, M. K., Wotzlaw, J.-F., Lai, Y.-J., Yamaguchi, A., & Schönbächler, M. (2019). Mesosiderite formation on asteroid 4 Vesta by a hit-and-run collision. *Nature Geoscience*, *12*(7), 510–515. https://doi.org/10.1038/s41561-019-0377-8

Hakim, K., Spaargaren, R., Grewal, D. S., Rohrbach, A., Berndt, J., Dominik, C., & van Westrenen, W. (2019). Mineralogy, structure, and habitability of carbon-enriched rocky exoplanets: A laboratory approach. *Astrobiology*, *19*(7), 867–884. https://doi.org/10.1089/ast.2018.1930

Hardersen, P. S., Cloutis, E. A., Reddy, V., Mothé-Diniz, T., & Emery, J. P. (2011). The M-/X-asteroid menagerie: Results of an NIR spectral survey of 45 main-belt asteroids. *Meteoritics & Planetary Sciences*, *46*(12), 1910–1938. https://doi.org/10.1111/j.1945-5100.2011.01304.x

Haughton, D. R., Roeder, P. L., & Skinner, B. J. (1974). Solubility of sulfur in mafic magmas. *Economic Geology*, *69*(4), 451–467. https://doi.org/10.2113/gsecongeo.69.4.451

Jennings, E. S., & Holland, T. J. B. (2015). A simple thermodynamic model for melting of peridotite in the system NCFMASOCr. *Journal of Petrology*, *56*(5), 869–892. https://doi.org/10.1093/petrology/egv020

Johnson, B. C., Sori, M. M., & Evans, A. J. (2020). Ferrovolcanism on metal worlds and the origin of pallasites. In *Nature astronomy*, (Vol. 4(1), pp. 41–44). Nature Research. https://doi.org/10.1038/s41550-019-0885-x

Jorritsma, J., & van Westrenen, W. (2025). *Iterative model of the chemical and physical interior of differentiated planetesimals [excel model]*. Mendeley Data, V1. https://doi.org/10.17632/sbdxrws596.1

Kim, Y., & Hirabayashi, M. (2022). A numerical approach using a finite element model to constrain the possible interior layout of (16) psyche. *Planetary Science Journal*, *3*(5), 122. https://doi.org/10.3847/PSJ/ac6b39

Landsman, Z. A., Emery, J. P., Campins, H., Hanuš, J., Lim, L. F., & Cruikshank, D. P. (2018). Asteroid (16) psyche: Evidence for a silicate regolith from spitzer space telescope spectroscopy. *Icarus*, *304*, 58–73. https://doi.org/10.1016/j.icarus.2017.11.035

Li, J., Mao, H. K., Fei, Y., Gregoryanz, E., Eremets, M., & Zha, C. S. (2002). Compression of Fe 3 C to 30 GPa at room temperature. *Physics and Chemistry of Minerals*, *29*(3), 166–169. https://doi.org/10.1007/s00269-001-0224-4

Libourel, G., Beck, P., Nakamura, A. M., Vernazza, P., Ganino, C., & Michel, P. (2023). V-type asteroids as the origin of mesosiderites. *Planetary Science Journal*, *4*(7), 123. https://doi.org/10.3847/PSJ/ace114

Lucas, M. P., Dygert, N., Ren, J., Hesse, M. A., Miller, N. R., & McSween, H. Y. (2020). Evidence for early fragmentation-reassembly of ordinary chondrite (H, L, and LL) parent bodies from REE-in-two-pyroxene thermometry. *Geochimica et Cosmochimica Acta*, *290*, 366–390. https://doi.org/10.1016/j.gca.2020.09.010

Magri, C., Nolan, M. C., Ostro, S. J., & Giorgini, J. D. (2007). A radar survey of main-belt asteroids: Arecibo observations of 55 objects during 1999–2003. *Icarus*, *186*(1), 126–151. https://doi.org/10.1016/j.icarus.2006.08.018

McClintock, W. E., Izenberg, N. R., Holsclaw, G. M., Blewett, D. T., Domingue, D. L., Head, J. W., et al. (2008). Spectroscopic observations of mercury's surface reflectance during messenger's first Mercury flyby. *Science*, *321*(5885), 62–65. https://doi.org/10.1126/science.1159933

McCoy, T. J., Dickinson, T. L., & Lofgren, G. E. (1999). Partial melting of the Indarch (EH4) meteorite: A textural, chemical, and phase relations view of melting and melt migration. *Meteoritics & Planetary Sciences*, *34*(5), 735–746. https://doi.org/10.1111/j.1945-5100.1999.tb01386.x

Meco, H., & Napolitano, R. E. (2005). Liquidus and solidus boundaries in the vicinity of order–disorder transitions in the Fe–Si system. *Scripta Materialia*, *52*(3), 221–226. https://doi.org/10.1016/j.scriptamat.2004.09.026

Montes-Arango, A. M., Marshall, L. G., Fortes, A. D., Bordeaux, N. C., Langridge, S., Barmak, K., & Lewis, L. H. (2016). Discovery of process-induced tetragonality in equiatomic ferromagnetic FeNi. *Acta Materialia*, *116*, 263–269. https://doi.org/10.1016/j.actamat.2016.06.050

Mysen, B. O., Virgo, D., & Seifert, F. A. (1982). The structure of silicate melts: Implications for chemical and physical properties of natural magma. *Reviews of Geophysics*, *20*(3), 353–383. https://doi.org/10.1029/RG020i003p00353

Neufeld, J. A., Bryson, J. F. J., & Nimmo, F. (2019). The top-down solidification of iron asteroids driving Dynamo evolution. *Journal of Geophysical Research: Planets*, *124*(5), 1331–1356. https://doi.org/10.1029/2018JE005900

Nichols-Fleming, F., Evans, A. J., Johnson, B. C., & Sori, M. M. (2022). Porosity evolution in metallic asteroids: Implications for the origin and thermal history of asteroid 16 psyche. *Journal of Geophysical Research: Planets*, *127*(2). https://doi.org/10.1029/2021JE007063

Nichols-Fleming, F., Evans, A. J., Johnson, B. C., & Sori, M. M. (2024). Moment of inertia and tectonic record of asteroid 16 psyche May reveal interior structure and core solidification processes. *Journal of Geophysical Research: Planets*, *129*(7), e2024JE008291. https://doi.org/10.1029/2024JE008291

O'Neill, H. S. C., & Palme, H. (2008). Collisional erosion and the non-chondritic composition of the terrestrial planets. *Philosophical Transactions of the Royal Society A: Mathematical, Physical and Engineering Sciences*, *366*(1883), 4205–4238. https://doi.org/10.1098/rsta.2008.0111

Pachmayr, U., Fehn, N., & Johrendt, D. (2016). Structural transition and superconductivity in hydrothermally synthesized FeX (X = S, Se). *Chemical Communications*, *52*(1), 194–197. https://doi.org/10.1039/C5CC07739G

Polanskey, C. A., Elkins-Tanton, L., Jaumann, R., Lawrence, D. J., Marsh, D. M., Moore, R. R., et al. (2018). Psyche science operations concept: Maximize reuse to minimize risk. In *SpaceOps conference*. https://doi.org/10.2514/6.2018-2703

Pollack, H. W. (1998). *Materials science and metallurgy* (4th ed.). Prentice-Hall.

Raducan, S. D., Davison, T. M., & Collins, G. S. (2020). Morphological diversity of impact craters on asteroid (16) psyche: Insight from numerical models. *Journal of Geophysical Research: Planets*, *125*(9), e2020JE006466. https://doi.org/10.1029/2020JE006466

Rai, N., & van Westrenen, W. (2014). Lunar core formation: New constraints from metal–silicate partitioning of siderophile elements. *Earth and Planetary Science Letters*, *388*, 343–352. https://doi.org/10.1016/j.epsl.2013.12.001

Sanchez, J. A., Reddy, V., Shepard, M. K., Thomas, C., Cloutis, E. A., Takir, D., et al. (2016). Detection of rotational spectral variation on the M-type asteroid (16) psyche. *The Astronomical Journal*, *153*(1), 29. https://doi.org/10.3847/1538-3881/153/1/29

Scheinberg, A., Elkins-Tanton, L. T., Schubert, G., & Bercovici, D. (2016). Core solidification and dynamo evolution in a mantle-stripped planetesimal. *Journal of Geophysical Research: Planets*, *121*(1), 2–20. https://doi.org/10.1002/2015JE004843

Scott, H. P., Huggins, S., Frank, M. R., Maglio, S. J., Martin, C. D., Meng, Y., et al. (2007). Equation of state and high-pressure stability of Fe3P-schreibersite: Implications for phosphorus storage in planetary cores. *Geophysical Research Letters*, *34*(6), L06302. https://doi.org/10.1029/2006GL029160

Shepard, M. K., de Kleer, K., Cambioni, S., Taylor, P. A., Virkki, A. K., Rívera-Valentin, E. G., et al. (2021). Asteroid 16 psyche: Shape, features, and global map. *The Planetary Science Journal*, *2*(4), 125. https://doi.org/10.3847/PSJ/abfdba

Shepard, M. K., Richardson, J., Taylor, P. A., Rodriguez-Ford, L. A., Conrad, A., de Pater, I., et al. (2017). Radar observations and shape model of asteroid 16 psyche. *Icarus*, *281*, 388–403. https://doi.org/10.1016/j.icarus.2016.08.011

Shepard, M. K., Taylor, P. A., Nolan, M. C., Howell, E. S., Springmann, A., Giorgini, J. D., et al. (2015). A radar survey of M- and X-class asteroids. III. Insights into their composition, hydration state, & structure. *Icarus*, *245*, 38–55. https://doi.org/10.1016/j.icarus.2014.09.016

Shepard, M. K., Timerson, B., Scheeres, D. J., Benner, L. A. M., Giorgini, J. D., Howell, E. S., et al. (2018). A revised shape model of asteroid (216) Kleopatra. *Icarus*, *311*, 197–209. https://doi.org/10.1016/j.icarus.2018.04.002

Steenstra, E. S., Sitabi, A. B., Lin, Y. H., Rai, N., Knibbe, J. S., Berndt, J., et al. (2017). The effect of melt composition on metal-silicate partitioning of siderophile elements and constraints on core formation in the angrite parent body. *Geochimica et Cosmochimica Acta*, *212*, 62–83. https://doi.org/10.1016/j.gca.2017.05.034

Steenstra, E. S., & van Westrenen, W. (2018). A synthesis of geochemical constraints on the inventory of light elements in the core of Mars. *Icarus*, *315*, 69–78. https://doi.org/10.1016/j.icarus.2018.06.023

Steenstra, E. S., & van Westrenen, W. (2020). Geochemical constraints on core-mantle differentiation in Mercury and the aubrite parent body. *Icarus*, *340*, 113621. https://doi.org/10.1016/j.icarus.2020.113621

Steinberg, T. A., Kurtz, J., & Wilson, D. B. (1998). The solubility of oxygen in liquid iron oxide during the combustion of iron rods in high-pressure oxygen. *Combustion and Flame*, *113*(1–2), 27–37. https://doi.org/10.1016/S0010-2180(97)00165-X

Stewart, A. J., van Westrenen, W., Schmidt, M. W., & Günther, D. (2009). Minor element partitioning between fcc Fe metal and Fe–S liquid at high pressure: The role of crystal lattice strain. *Earth and Planetary Science Letters*, *284*(3–4), 302–309. https://doi.org/10.1016/J.EPSL.2009.04.040

Tarduno, J. A., Cottrell, R. D., Nimmo, F., Hopkins, J., Voronov, J., Erickson, A., et al. (2012). Evidence for a dynamo in the main group pallasite parent body. *Science*, *338*(6109), 939–942. https://doi.org/10.1126/science.1223932

Tholen, D. J. (1984). *PhD dissertation: Asteroid taxonomy from cluster analysis of photometry*. University of Arizona. Retrieved from http://hdl.handle.net/10150/187738

Vočadlo, L., Knight, K. S., Price, G. D., & Wood, I. G. (2002). Thermal expansion and crystal structure of FeSi between 4 and 1173 K determined by time-of-flight neutron powder diffraction. *Physics and Chemistry of Minerals*, *29*(2), 132–139. https://doi.org/10.1007/s002690100202

Weiss, B. P., Merayo, J. M. G., Ream, J. B., Oran, R., Brauer, P., Cochrane, C. J., et al. (2023). The Psyche magnetometry investigation. In *Space science reviews* (Vol. 219(3). 22, Springer Science and Business Media B.V. https://doi.org/10.1007/s11214-023-00965-z

Williams, Q. (2009). Bottom-up versus top-down solidification of the cores of small solar system bodies: Constraints on paradoxical cores. *Earth and Planetary Science Letters*, *284*(3–4), 564–569. https://doi.org/10.1016/J.EPSL.2009.05.019

Yu, X., & Ji, Z. (2017). Grain boundary in oxide scale during high-temperature metal processing. In *Study of grain boundary character*. InTech. https://doi.org/10.5772/66211

Zaitsev, A. I., Dobrokhotova, Z. V., Litvina', A. D., & Mogutnov, B. M. (1995). Thermodynamic properties and phase equilibria in the Fe-P system. *Journal of the Chemical Society Faraday Transactions*, *91*(4), 703–712. https://doi.org/10.1039/ft9959100703

Zhang, Z., Bercovici, D., & Elkins-Tanton, L. (2022). Cold compaction and macro-porosity removal in rubble-pile asteroids: 1. Theory. *Journal of Geophysical Research: Planets*, *127*(10). https://doi.org/10.1029/2022JE007342

Zuber, M. T., Park, R. S., Elkins-Tanton, L. T., Bell, J. F., Bruvold, K. N., Bercovici, D., et al. (2022). The psyche gravity investigation. In *Space science reviews* (Vol. 218(8). 57, Springer Science and Business Media B.V. https://doi.org/10.1007/s11214-022-00905-3